Busby, C. J., Tamura, Y., Blum, P., Guerin, G., Andrews, G. D. M., Barker, A. K., ... Yang Yang, A. (2017). The missing half of the subduction factory: shipboard results from the Izu rear arc, IODP Expedition 350. *International Geology Review*, *59*(13), 1677-1708. https://doi.org/10.1080/00206814.2017.1292469

MS ID # TIGR-2017-0029

THE MISSING HALF OF THE SUBDUCTION FACTORY: SHIPBOARD RESULTS FROM THE IZU REAR ARC, IODP EXPEDITION 350

C.J. Busby, Y. Tamura, P. Blum, G. Guèrin, G.D.M. Andrews, A.K. Barker, J.L.R. Berger, E.M. Bongiolo, M. Bordiga, S.M. DeBari, J.B. Gill, C. Hamelin, J. Jia, E.H. John, A.-S. Jonas, M. Jutzeler, M.A.C. Kars, Z.A. Kita, K. Konrad, S.H. Mahoney, M. Martini, T. Miyazaki, R.J. Musgrave, D.B. Nascimento, A.R.L. Nichols, J.M. Ribeiro, T. Sato, J.C. Schindlbeck, A.K. Schmitt, S.M. Straub, M.J. Vautravers, Yamashita, M., and Y. Yang

ABSTRACT

IODP Expedition 350 was the first to be drilled in the rear part of the Izu-Bonin, although several sites had been drilled in the arc axis to fore-arc region; the scientific objective was to understand the evolution of the Izu rear arc, by drilling a deepwater volcaniclastic section with a long temporal record (Site U1437). The Izu rear arc is dominated by a series of basaltic to dacitic seamount chains up to ~100 km long roughly perpendicular to the arc front. Dredge samples from these are geochemically distinct from arc front rocks, and drilling was undertaken to understand this arc asymmetry. Site U1437 lies in a ~20 km-wide basin between two rear arc seamount chains, ~90 km west of the arc front, and was drilled to 1804 mbsf with excellent recovery. We expected to drill a volcaniclastic apron, but the section is much more mud-rich than expected (~60%), and the remaining fraction of the section is much finer-grained than predicted from its

position within the Izu arc, composed half of ashes/tuffs, and half of lapilli tuffs of fine grain size (clasts <3 cm). Volcanic blocks (>6.4 cm) are only sparsely scattered through the lowermost 25% of the section, and only one igneous unit was encountered, a rhyolite peperite intrusion at ~1390 mbsf. The lowest biostratigaphic datum is at 867 mbsf (~6.5 Ma), the lowest paleomagnetic datum is at ~1300 mbsf (~9 Ma), and the rhyolite peperite at ~1390 mbsf has yielded a U-Pb zircon concordia intercept age of 13.6 +1.6/-1.7 Ma.

Both arc front and rear arc sources contributed to the fine-grained (distal) tephras of the upper 1320m, but the coarse-grained (proximal) volcaniclastics in the lowest 25% of the section are geochemically similar to the arc front, suggesting arc asymmetry is not recorded in rocks older than ~13 Ma.

Keywords: International Ocean Discovery Program, Izu-Bonin-Marianas Arc, island arcs, magmatic arcs, rear arc, Japanese volcanoes

INTRODUCTION

This paper provides an overview of shipboard results from one of three closely related International Ocean Discovery Program (IODP) expeditions carried out in sequence in the Izu-Bonin-Mariana (IBM) arc system in 2014 (Figure 1). It is meant to reach a wider audience than the scientific ocean drilling community, by presenting shipboard results in a compact and accessible manner, focusing on geologic results that will be of interest to those working in magmatic arcs on continents as well as those in the sea. More sophisticated geochemical results will be reported in future papers, using shore-based techniques; this paper focuses on geologic observations, which will not

change. on the basis We refer those seeking much greater detail to the *Proceedings of the International Ocean Discovery Program, Expedition 350*; all of the figures presented here appear in that volume, along with hundreds more (Tamura et al., 2015).

Expedition 350 was the first expedition to drill in the Izu rear arc; all previous IODP/ODP sites were drilled in or near the Izu-Bonin arc front or fore-arc (Figure 2), leading to an incomplete view of Izu arc magmatism. Thus, the main objective of Expedition 350 was to reveal the history of "the missing half" of the subduction factory (Tamura et al., 2013). The second expedition (351) focused on IBM arc origins by drilling west of the Kyushu-Palau Ridge (Figure 1), where it was inferred that the foundation, origin, and early evolution of the IBM arc are recorded (Arculus et al., 2013, 2015). The third expedition (352) examined the processes of subduction initiation, by drilling the outer IBM fore-arc (Figure 1; Pearce et al., 2013, 2015).

The goal of Expedition 350 was to core and log one site on the Izu rear arc, Site U1437 (Figure 1). This site was chosen to provide a temporal record of rear-arc magma compositions, ideally from Paleogene to Neogene time, allowing comparison with the previously drilled fore-arc magmatic record and determination of across-arc geochemical variations throughout the history of the arc system. In addition to drilling in the rear arc, Expedition 350 also drilled a 150 m deep geotechnical hole in the fore-arc (Site U1436, Figure 1) for potential deep drilling; this site was chosen partly on the basis of results gotten from ODP Site 792, which is only 1.5 to the east of site U1436 (Tamura et al., 2015a). ODP Site 792 was drilled to 886 meters below the sea floor (mbsf,) and the stratigraphy of its upper 150 m (Taylor et al., 1990) is very similar to that of Site U1436. Core from these sites yielded a rich record of Late Pleistocene explosive volcanism, but

70 is not discussed further here, for space considerations. This paper focuses on Site U1437,
71 which was cored at 1776 meters below sea level (mbsl) to a depth of 1806.5 mbsf,
72 through a volcaniclastic succession, with excellent core recovery (Holes U1437 B, D and
73 E overall: 55%, 74% and 62%). This provided a time-integrated view of the rear arc over
74 the past ~14 myr.
75 Major questions addressed by drilling the Izu rear arc include the following: (1)
76 Izu rear arc volcanoes differ from arc front volcanoes by being more similar to averaged
77 continental crust (i.e., enriched in alkalis, Ba, Th, U and LREE). The Izu rear arc is
78 therefore important for understanding how arc magmas and intracrustal differentiation
79 produces crust that is similar in composition to the "averaged continental crust." When
80 did this arc asymmetry develop? (2) What kinds of basins accommodated the
81 volcaniclastic succession we drilled? (3) What eruption, transport and depositional
82 processes are recorded in the rear arc volcaniclastic succession targeted for drilling, and
83 what kinds of depositional environments are represented by the succession?
84
85 **EVOLUTION OF THE IBM ARC SYSTEM**
86 The IBM arc (Figure 1) formed in response to subduction of the Pacific plate over
87 the past 52 myr (Stern et al., 2003). Subduction began as part of a hemisphere-scale
88 foundering of old, dense lithosphere in the western Pacific (Bloomer et al., 1995; Cosca
89 et al., 1998). During the subduction initiation stage (~52–47 Ma) investigated by
90 Expedition 352 (Figure 1), igneous activity successively produced low-K mid-ocean-
91 ridge basalt (MORB)-like tholeiite, boninite, and subordinate low-K rhyolite across the
92 region that now lies in the fore-arc (cf. Reagan et al., 2015). This suggests that sinking of

93 the downgoing plate was rapidly followed by an episode of asthenospheric upwelling and
94 melting, sometimes enhanced by solute-bearing water fluxes released from the
95 downgoing plate, over a zone that was thousands of kilometers long and as wide as 200
96 km (Reagan et al., 2010). As subduction proceeded, hydrous mantle melting overprinted
97 decompression mantle melting, establishing the first mature arc in Eocene to Oligocene
98 time, referred to as the Kyushu-Palau arc (Taylor, 1992; Ishizuka et al., 2006a, 2006b,
99 2011), herein also referred to as the Paleogene arc.

100 By ~25 Ma, rifting began along the length of the Kyushu-Palau arc and opening
101 of the Shikoku Basin isolated the rear-arc volcanoes from the arc-front volcanoes
102 (Ishizuka et al., 2011; Figure 1), producing the Kyushu-Palau Ridge remnant arc, which
103 has Eocene and Oligocene rear-arc rocks (see Expedition 351 site, Figure 1). Seafloor
104 spreading of the Shikoku and Parece Vela Basins (Figure 1) at ~25–17 Ma was likely
105 accompanied by a hiatus in arc magmatism, but the fore-arc sedimentary record shows
106 that arc-front volcanism resumed by ~17 Ma (Stern et al., 2003), referred to as the
107 Neogene arc, or the IBM arc (Ishizuka et al., 2011).

108 The Neogene IBM arc front is inferred to lie in nearly the same position as the
109 Paleogene arc front (Ishizuka et al., 2011); however, pre-Quaternary rocks have not been
110 recovered from the IBM arc front, perhaps because they are buried or were partly
111 remelted and/or remobilized during the Quaternary. In contrast, the Izu rear arc (Figures,
112 1, 3) has not been extensively buried or modified by Quaternary magmatic processes, so
113 Neogene rocks are well preserved; these are dominated by ~17 to 3 Ma northeast-
114 trending rear-arc seamount chains described below. The Marianas segment of the IBM
115 arc (Figure 1) differs from the Izu segment by lacking the rear-arc seamount chains;

instead, a new episode of arc rifting began at ~7 Ma, resulting in opening of the Mariana Trough back-arc basin by seafloor spreading at ~3–4 Ma (Yamazaki and Stern, 1997). Rifting of the Izu arc began at ~3 Ma behind the arc front (Figure 3).

We know more about the Neogene history of the IBM arc than we do about its Paleogene history; yet it is thought that most of the IBM crust was generated in the Paleogene (Eocene–Oligocene; Kodaira et al., 2008). Furthermore, silicic volcanoes of the Quaternary arc front and Miocene granitic rocks in the Izu collision zone on Honshu are inferred to have formed by melting of Eocene–Oligocene arc crust (Tamura et al., 2009, 2010). As discussed below, Neogene rhyolite volcanism may be more important in the Izu rear-arc seamount chain than previously thought and could have resulted from melting of Paleogene "arc basement." For this reason, we will now review the evidence for Paleogene arc basement highs in the Izu arc and discuss constraints on their age and origin.

PALEOGENE ARC BASEMENT HIGHS IN THE IZU ARC

Magnetic and seismic surveys indicate that both IODP Sites U1436 and U1437 lie along buried north–south ridges that consist of magmatic crystalline rocks, which are inferred to be Oligocene–Eocene (Paleogene) in age. Three conspicuous, approximately north–south rows of long-wavelength magnetic anomalies were identified by Yamazaki and Yuasa (1998) in the Izu-Bonin arc system and attributed to loci of middle- to lower-crustal magmatic bodies (Figure 1):

- The western north–south anomaly corresponds to the Kyushu-Palau Ridge, where Eocene and Oligocene lava was dredged; these have rear-arc geochemical affinity, and

139 are interpreted as as rear-arc magmas rifted off the Paleogene arc during the opening of
140 the Shikoku Basin (Ishizuka et al., 2011; Kodaira et al., 2008).
141 • The eastern north–south anomaly lies in the modern fore-arc near the arc front and
142 corresponds to the Shin-Kurose Ridge (Figure 1) (Yamazaki and Yuasa, 1998), also
143 referred to as the Izu fore-arc high (Taylor, Fujioka, et al., 1990). The Shin-Kurose
144 Ridge/fore-arc high forms a bathymetric high in the northern Izu arc and is buried
145 beneath Oligocene to Quaternary volcaniclastic and sedimentary rocks in the southern Izu
146 arc, at Ocean Drilling Program (ODP) Site 792 and Site U1436. Andesite lava in the
147 lowermost 82 m at Site 792 was referred to as "Oligocene basement," on the basis of
148 K/Ar ages (Taylor, Fujioka, et al., 1990; Taylor, 1992), but more recent $^{40}Ar/^{39}Ar$ dating
149 show these are Eocene (Ishizuka et al., 2011).
150 • The central north–south magnetic anomaly lies buried in the Izu rear arc (Figure 1) and
151 is referred to as the Nishi-shichito Ridge (Figure 4) (Yamazaki and Yuasa, 1998). This
152 basement high has not been drilled and was one of the objectives of Expedition 350.
153 Kodaira et al. (2008) ran a wide-angle seismic profile along the length of the rear-arc
154 Nishi-shichito Ridge and compared it to a wide-angle seismic profile made along the
155 length of the arc front by Kodaira et al. (2007a, 2007b) (Figure 4). They divided the arc
156 front into segments based on variations in the thickness of middle crust and did the same
157 for the rear-arc Nishi-shichito Ridge. They concluded that although the thickness of the
158 middle crust for each rear-arc segment is smaller than the thickness in the arc front, the
159 bulk compositions of the crust segments are inferred to be the same, on the basis of
160 seismic properties.. Furthermore, they used the match on middle crustal thicknesses to
161 infer that the Nishi-shichito Ridge is a "paleo-arc" that obliquely rifted off the arc front in

an extension direction parallel to the northeast–southwest Sofugan Tectonic Line (Figure 1). The Sofugan Tectonic Line is the boundary between the Izu and Bonin arc segments (Figure 1); south of it lies the prominent Bonin Ridge and the deep fault-bounded Ogasawara Trough to the west, produced by Eocene to early Oligocene arc magmatism and back-arc extension, respectively. Both the prominent arc ridge and the fault-controlled back-arc basin are absent north of the Sofugan Tectonic Line, so we infer that the Sofugan Tectonic Line originated as an accommodation fault between a region of high extension to the south and little or no extension to the north. Kodaira et al. (2008) propose that oblique rifting of the Nishi-shichito Ridge paleoarc off the arc front occurred during the opening of the Shikoku Basin, sometime after ~30 Ma. If the oblique rifting model is correct, the crystalline basement beneath Site U1437, not reached during Expedition 350, may represent rear-arc crust but formed in a position much closer to the arc front than it is now; alternatively, it may represent arc-front crust that has become stranded in the rear arc by rifting. New seismic surveys undertaken in preparation for drilling at Site U1437, described below, also support the interpretation that the rear arc is underlain by Paleogene arc basement rocks.

NEOGENE REAR-ARC VOLCANISM, IZU ARC

We refer to all Neogene volcanic rocks behind the Izu arc front as rear-arc volcanic rocks. Rear-arc volcanic rocks (Figure 3) include (1) the ~17–3 Ma east northeast–trending basaltic to rhyolitic rear-arc seamount chains, (2) the <3 Ma bimodal back-arc knolls of the broad extensional zone, and (3) the <1.5 Ma bimodal volcanic rocks of the active rift immediately behind the arc front. Thus, Izu rear-arc volcanism

185 falls into two magmatic suites: the <3 Ma bimodal rift-type magmas and the ~17–3 Ma
186 basalt to rhyolite rear-arc seamount-type magmas. Both types lie within the rear part of
187 the arc (i.e., behind the arc front) and lie on arc crust, although the westernmost end of
188 the rear-arc seamount chains lies on Shikoku Basin oceanic crust. The bimodal rift-type
189 magmas differ from both the arc front and the rear-arc seamount chains in trace element
190 and radiogenic isotopic ratios; this has been variably attributed to (1) a transition from
191 flux to decompression mantle melting as arc rifting commences, (2) a change in the
192 character of slab-derived flux, or (3) a change in the mantle source through mantle wedge
193 convection (Hochstaedter et al., 1990a, 1990b, 2001; Ishizuka et al., 2003a, 2006b;
194 Tollstrup et al., 2010).

195 The Izu rear-arc seamount chains are as long as ~80 km and strike N60°E (Figure
196 3). The tops of the Izu rear-arc volcanic chains were sampled by dredging, and their
197 compositions range from basalt to rhyolite (Ishizuka et al., 1998, 2003b; Hochstaedter et
198 al., 2000). Three main hypotheses have been proposed for the origin of the seamount
199 chains:

200 1. They are related to compression caused by collision between the southwest
201 Japan and Izu arcs, associated with opening of the Japan Sea (Karig and Moore, 1975a;
202 Bandy and Hilde, 1983).

203 2. They formed along Shikoku Basin transform faults (Yamazaki and Yuasa,
204 1998).

205 3. They overlie diapirs in the mantle wedge, such as the “hot fingers” proposed
206 for northeast Japan (Tamura et al., 2002), illustrated in Figure 5.

A striking characteristic of volcanic arcs is the asymmetry in geochemical characteristics with distance from the trench, which was known prior to the advent of plate tectonics (Kuno, 1959; Dickinson and Hatherton, 1967). Izu arc-front rocks are low-K, but the rear-arc type lava is medium to high-K (Gill, 1981). Similarly, arc-front volcanic rocks are strongly depleted in incompatible light rare earth elements (REEs) relative to the middle and heavy REEs, whereas lava from rear-arc seamount chains is enriched in light REEs. On both K_2O versus SiO_2 and REE plots, the composition of the rear-arc seamount chain magmas is more similar to the continental crust composition than the arc-front magmas. Thus, the Izu rear-arc magmatism and crust formation appears to be a better analog to generate continental crust than the arc front (Tamura et al., 2013).

Site U1437 lies in a ~20 km wide basin in the low area between two major constructional volcanic ridges: the Manji and Enpo rear-arc seamount chains (Figure 3). It is therefore classified as a volcano-bounded intra-arc basin, using the criteria elucidated by Smith and Landis (1995) (Figure 6). In contrast, the active rift to the east of Site U1437 (Figure 3) is a fault-bounded intra-arc basin, using the terminology of Smith and Landis (1995) (Figure 6). For simplicity, the volcano-bounded basin bounded by the Enpo and Manji rear-arc seamount chains (Figure 7) is referred to as the Enpo-Manji volcano-bounded basin (Figure 8C, 8D). Similarly, we propose that future workers refer to other basins between rear-arc seamount chains by the names of the chains that bound them (e.g., Genroku-Enpo Basin and Manji-Kan'ei Basin, Figure 3).

NEW DESCRIPTIVE SCHEME FOR VOLCANICLASTIC ROCKS

Expedition 350 devised a new scheme for describing volcaniclastic and associated nonvolcaniclastic sediments, described in detail by Tamura et al. (2015b). The new scheme was devised to improve description of volcaniclastic sediments and their mixtures with nonvolcanic (siliciclastic, chemical, and biogenic) sediments but maintain the usefulness of prior schemes for describing nonvolcanic sediments. The new scheme was devised to facilitate the understanding of volcano-sedimentary processes by making reproducible and quantifiable observations of volcanic input to the sedimentary record. Previous core descriptions (e.g. ODP Leg 126) obscured the importance of volcanic input by referring to volcanic material (e.g. ashes/tuffs) as siliclastic material (e.g, sands/sandstone or tuffaceous sands/sandstones). The new classification scheme is based entirely on observations that can be made by any scientist at the macroscopic and microscopic level, making the data more reproducible from user to user. Genetic inferences are not part of the descriptive scheme but can be added as comments to descriptive records if so desired. A very brief description of the scheme is presented here to allow the reader to understand our rock descriptions.

Four sedimentary lithologic classes were defined, including: 1. Volcanic lithologic class, defined as >75% volcanic particles. 2. Tuffaceous lithologic class, containing 25%–75% volcanic-derived particles mixed with nonvolcanic particles. 3. Nonvolcanic siliciclastic lithologic class, containing <25% volcanic siliciclastic particles, where nonvolcanic siliciclastic particles dominate chemical and biogenic particles. 4. Biogenic lithologic class, containing <25% volcanic and nonvolcaniclastic siliciclastic and chemical particles. The principal name for sediments and sedimentary rocks is based on grain size and is purely descriptive; it does not depend on interpretations of

252 fragmentation, transport, or depositional or alteration processes. The sedimentary grain
253 size classes of Wentworth (1922) are used for the nonvolcanic siliciclastic and tuffaceous
254 lithologic classes, whereas the grain size classes of Fisher and Schmincke (1984) are used
255 for the volcanic lithologic class. The prefix "monomict" was applied where clast
256 compositions were restricted to a single type and "polymict" was applied where clast
257 compositions of multiple types were present. We adopted a new method to estimate the
258 compositional range of volcanic clasts using three entries: "mafic," "evolved" and a
259 mixture of the two, termed "bimodal." In our macroscopic analyses, mafic versus evolved
260 intervals were defined by the grayscale index of the main particle component, with mafic
261 grains and clasts usually ranging from black to dark gray and evolved grains and clasts
262 ranging from dark gray to white. Microscopic examination further aided in assigning the
263 prefix "mafic" or "evolved", using glass shard color and mineralogy. Intervals we
264 described as mafic are inferred to be basalt and basaltic andesite, and intervals we
265 described as evolved were inferred to be intermediate and silicic in composition;
266 however, precise determination of bulk composition requires chemical analysis.
267 In summary, the new volcaniclastic descriptive scheme applied during Expedition
268 350 uses a more nongenetic approach than proposed by previous authors because the
269 sediments and rocks are named based on materials that are visible macroscopically and
270 microscopically and not on the basis of inferred fragmentation, transport, and
271 depositional processes (i.e., pyroclasts, autoclasts, hydroclasts, epiclasts, and reworked
272 volcanic clasts [Fisher and Schmincke, 1984; Cas and Wright, 1987; McPhie et al.,
273 1993]).
274

IODP SITE U1437

Site U1437 is located in the Izu rear arc and is ~330 km west of the axis of the Izu-Bonin Trench (Figures 1, 2) and ~90 km west of the arc-front volcanoes Myojinsho and Myojin Knoll (Figure 3) at 2117 meters below sea level between the Manji and Enpo seamount chains (Figure 7). The stratigraphic section shown in Figure 9 is a composite from three holes drilled a few tens of meters apart using different techniques. The shallowest and least consolidated material was penetrated at Hole U1437B (drilled using Advanced Piston Coring (APC), Half-Length Advanced Piston Corer (HLAPC), and Extended Core Barrel (XCB). Deeper, more consolidated units were drilled at Holes U1437D and U1437E using the Rotary Core Barrel (RCB) (see http://iodp.tamu.edu/tools/ for details about these tools). These different drilling techniques resulted in partial sampling of the section: In Hole U1437B we cored 439.1 m and recovered 242.6 m (55% recovery). In Hole U1437D we cored 677.4 m, with 503.8 m recovered (74%). In Hole U1437E we cored 702.5 m and recovered 387.45 m (55% recovery). Incomplete and disturbed cores are unfortunate but expected; to ensure a more uniform perspective on the section (including intervals that are not recovered in cores), downhole logging was carried out before the hole is cased. Combined studies of cores and well logs allowed the entire sequence to be interrogated. Most of the unconsolidated stratigraphy in Hole U1347B is well preserved and few coring disturbances (Jutzeler et al. 2014) occur, allowing very good stratigraphic continuity. Drilling disturbances are present in Holes U1347D and U1347E, and vary depending on rock type and consolidation.

Seismic Surveys

Seismic surveys for Site U1437 are summarized briefly here. Numerous lines were shot in two different campaigns (Yamashita et al., 2017); parts of three seismic sections that cross at Site U1437 are plotted on Figure 7C and shown in Figure 8. Line IBr5 (Figure 8A) is the longest seismic line, running east–west from the Manji rear-arc seamount chain across the Enpo seamount chain to the arc front; it was shot both by wide-angle ocean-bottom seismometer (OBS, Figure 8A) and by multichannel seismic (MCS, Figure 8B). The wide-angle OBS survey shows the velocity structure of the upper ~10 km, and the MCS line shows the upper ~5 km. Generally, the velocity transition to >5 km/s is thought to represent the transition to igneous rocks, perhaps representing arc upper crust lava or crystalline rocks, and the velocity transition to 6 km/s is generally thought to represent the transition to middle crust (see boundaries picked in Figure 8B). Tamura et al. (2013) estimated the 5 km/s iso-velocity contour to lie at ~2100 mbsf at Site U1437 and suggested that these rocks could be Oligocene–Eocene "igneous basement," consisting of lava and/or intrusions. Line IBM3-NW5 (Figure 8C) clearly shows that Site U1437 lies in a volcano-bounded basin between the Enpo and Manji rear-arc seamount chains.

Age Model

Site U1437 was drilled to a depth of 1804 mbsf in three holes (U1437B, U1437D, and U1437E), which we divide into seven lithostratigraphic units and one igneous unit (Figures 9 and 10). The biochronology for Site U1437 was established based on planktonic foraminifers and calcareous nannofossils (Figure 9). Both fossil groups show

321 that the upper 1403 m of the succession spans from the lower Pleistocene to the upper
322 Miocene (maximum age detectable was ~11–12 Ma), and the timing of bioevents agrees
323 well with magnetostratigraphic data. Deeper than 1403 mbsf, bioevents were difficult to
324 establish because of poor preservation and low microfossil abundance (Figure 9),
325 corresponding to a lithologic change from a succession dominated by tuffaceous
326 mud/mudstone to one dominated by volcanic material (Figure 10).

327 We infer that a normal fault at the base of Hole U1437D was responsible for
328 drilling problems there, including low recovery and more fractured rock. This forced us
329 to drill a new hole (Hole U1437E) which started at the same subbottom depth as the base
330 of Hole U1437D.; the first core was also fractured but cores below that were not. The
331 fault is not obvious in the seismic section (Figure 8C, 8D) but it is not excluded either.
332 On the basis of paleomagnetic results (Tamura et al. 2015a), this normal fault is inferred
333 to have caused a loss of section between the two holes (Figure 9). Magnetostratigraphy
334 could then be followed down as far as the top of Chron C4An (8.771 Ma) at 1302 mbsf
335 (Unit V, Figure 9). The age model does not extend into Units VI and VII (Figure 9)
336 because magnetostratigraphy was impossible to recognize, with the exception of reversed
337 polarity seen at 1389.35 mbsf in igneous Unit 1, which indicated that coring had
338 proceeded below the base of normal Chron C5n.2n (9.984–11.056 Ma; Tamura et al.
339 2015a) spanning the upper part of the lowest nannofossil age range. One additional age
340 control point was added immediately postcruise: Igneous Unit 1 is a rhyolite intrusive
341 sheet with peperite margins (at 1389 – 1390 mbsf, Figure 10), described further below,
342 which indicate that it is penecontemporaneous with the volcaniclastic section that
343 encloses it (Unit VI, Figure 10). In-situ measurement of zircons within magnetite crystals

344 in the rhyolite intrusion yielded a preliminary U-Pb age of 13.6 Ma ±1.7 (n = 9) (Schmitt,
345 pers. comm., 2014; Andrews et al., 2015; Konrad et al., 2016). Thus, we tentatively infer
346 that the age of units VI and VII is ca. 9 – 14 Ma.
347
348 **Description and Interpretation of Lithostratigraphic Units**
349 Lithostratigraphic Units I–VII (Figure 10) are distinguished from each other based
350 on the proportion and characteristics of tuffaceous mud/mudstone and interbedded tuff,
351 lapilli-tuff, and tuff-breccia. Visual description of core was supplemented by 13 smear
352 slides from Hole U1437B, and thin sections from Holes U1437B, U1437D, U1437E (5,
353 63 and 93, respectively). Mineralogy was done by macroscopic and microscopic
354 description; the shipboard XRD unit was not working so more detailed clay mineralogy
355 was not done. The tuffaceous mud/mudstone is strongly to intensely bioturbated.
356 Alteration becomes more pervasive and increases in intensity downhole; it is initially
357 predominantly glauconitic–smectitic and eventually becomes more chloritic. The
358 transition from unconsolidated to lithified rocks occurred progressively; however, the
359 change to RCB drilling provides a useful approximation of the transition between
360 unconsolidated sediment and sedimentary rock; on this basis the transition lies at 427
361 mbsf (bottom of Hole U1437B and top of Hole U1437D). Exact positions of the contacts
362 between lithostratigraphic units are given in Tamura et al. (2015a, 2015d).
363
364 Lithostratigraphic Unit I (0 to 682.12 mbsf)
365 Unit I is 0 to ~4.3 Ma in age (Figure 9), is 682.12 m thick, and consists largely
366 (88%) of mud/mudstone with 25%–75% dispersed ash, referred to as tuffaceous mud or

367 mudstone (depending on whether or not it is lithified; Figures 10, 11). The tuffaceous
368 mud/mudstone contains abundant fine colorless glass shards and rare crystals, plus
369 carbonate materials such as foraminifers. The rest of Unit I (12%) consists of ash or tuff
370 intervals (again depending on whether or not it is lithified), except for very rare (1.2%)
371 laplli-ash/lapilli tuff and lapillistone intervals with pumice or scoria <1 cm in size. The
372 ash/tuff lithofacies was mainly differentiated into two types, evolved (white to dark gray,
373 probably intermediate to silicic composition), or mafic (black, with brownish shards). A
374 small number of intervals were described as bimodal because they have both colorless
375 and brown-colored glass. The ashes/tuffs are mainly composed of glass shards (i.e., they
376 are vitric tuffs), although some are graded, with crystal-rich basal layers, commonly
377 plagioclase and pyroxene (Figure 11). Sedimentary structures include lamination and
378 bioturbation (Figure 11). Evolved ash/tuff intervals are four times as common as the
379 mafic ash/tuff intervals. Hornblende-bearing evolved ashes/tuffs, while rare (7%), have
380 elevated K_2O contents relative to most of the other ash/tuff intervals (geochemical
381 methods described in Tamura et al., 2015b); we suggest these record rear-arc seamount
382 volcanism rather than arc front or rift volcanism (geochemistry discussed further below).
383 Unit I has an unusually high sedimentation rate for fine-grained deep marine sediment far
384 from a continental margin and not associated with a deep-sea fan system; it is ~118
385 m/myr in the upper 230 m (0~2 Ma), and ~200 m/myr in the lower 450 m (2~4.3 Ma).
386 For more than 4 myr, this part of the Enpo-Manji basin collected mud with a high
387 ash component at a high rate, with volcaniclastic intervals consisting almost entirely of
388 ash/tuff limited to only 12% of the section. The sparseness, thinness, and fine grain size
389 of discrete volcaniclastic layers in lithostratigraphic Unit I is enigmatic, given that it

390 accumulated in close proximity to volcanoes of the active rift and back-arc knolls
391 extensional zone (<3 Ma) and rear-arc seamount chains (>3 Ma), in addition to lying
392 within 90 km of the arc front (Figures 1 and 3). The lateral continuity of reflectors in
393 Lithostratigraphic Unit I on the seismic section that lies transverse to the Enpo-Manji
394 basin (Figure 8C) is typical of fine-grained basinal deposits far from volcanic sources.
395 Based on features of the volcaniclastic intervals (evolved ash/tuff and mafic ash/tuff),
396 including sharp basal contacts, good sorting, and normal grading, we suggest deposition
397 by suspension settling through water, or by seafloor-hugging density currents, or some
398 combination (e.g., vertical density currents that transition into lateral density currents
399 when they reach the seafloor, in a manner envisioned by Carey [1997] and Manville and
400 Wilson [2004]). Thus, the ash/tuff intervals may represent ash falls from relatively distal
401 subaerial eruptions, which settled through water, and perhaps in some cases flowed along
402 the bottom as dilute density currents, and escaped reworking by bottom currents before
403 burial. The depositional process for the tuffaceous mud/mudstone that make up 88% of
404 Unit I is less well understood; it may be hemipelagic rain, dilute turbid flow, sediment
405 drift, or some combination thereof.
406
407 Lithostratigraphic Unit II (682.12 – 726.50 mbsf)
408 Unit II is ~4.3 – 4.4 Ma in age and is only 44.38 m thick (Figures 9, 10), but it
409 makes bright reflectors on the seismic profiles (Figure 8C, 8D). This is because it has
410 much more abundant volcaniclastics (~75%) and much less tuffaceous mudstone (~25%)
411 than is present in Units I or III. Additionally, the volcaniclastics in Unit II are coarser
412 grained than those in adjacent Units I and III (Figure 12), with pumice lapilli-tuff and

pumice lapillistone forming slightly more than half of the thickness, and tuff forming slightly less than half. The volcaniclastics in Unit II also differ from those of Units I and III by being entirely evolved (no mafic volcaniclastics present). The volcaniclastic intervals are planar bedded or cross bedded, and commonly show normal grading (Figure 12). They contain plagioclase, clinopyroxene, orthopyroxene and amphibole crystals in varying proportions. The tuffaceous mudstone is like that of Unit I but more lithified and altered to green clay minerals.

Unit II is dominated by monomictic pumice lapilli-tuff and lapillistone that is relatively well sorted, with abundant interstratified well-sorted crystal and vitric tuff, and is stratified, with planar and cross lamination, sharp bases, and graded bioturbated tops (Figure 12). We interpret it to represent the deposits of density current deposits, and the monomictic composition may indicate that at least some were eruption fed.

Lithostratigraphic Unit III (726.50 – 1017.88 mbsf)

Unit III is ~4.4 – 6.2 Ma in age (Figure 9), is 291.38 m thick, and is dominated by tuffaceous mudstone (~64%) and lesser tuff (~35%) (Figures 10, 13). Lapilli-tuff represents only ~1% of the unit. All intervals of tuff, and the rare lapilli-tuff, are compositionally evolved. Unit III shows an increase in fine-grained tuff (relative to tuffaceous mudstone) in its basal ~80 m; above that, Unit III is similar to Unit I, except that it lacks the mafic tuff that makes up ~20% of the tuff in Unit I. The tuffaceous mudstone intervals in Unit III have abundant bioturbation (Figure 13). The evolved tuffs of Unit III are of two main types: (1) dark gray tuffs identical to those of Units I and II, and not described further here; and (2) intercalated white to gray-green tuff, which is

much finer grained and better sorted, in places appearing chert-like, i.e. a dense very fine-grained siliceous material (Figure 13). This fine-grained tuff has laminations produced by alternation of glass shard–rich layers (white) and layers of mixed shards, pumice, and crystal fragments (gray-green), repeated over intervals up to several meters thick, with no bioturbation or tuffaceous mudstone interbeds. Thus, the intervals seem to record fairly continuous but pulsating sedimentation, probably from unsteady density currents, over a relatively short period of time for each interval (possibly days or weeks). The laminations commonly show soft-sediment deformation (Figure 13), supporting the interpretation that the intervals were deposited rapidly. Intercalated white to gray-green evolved tuff intervals form much of the volcaniclastics in the lower part of Unit III, where the volcaniclastic content is highest for this unit. The very large quantity of very fine glass shards in this facies suggests phreatomagmatic eruption, typified by extremely efficient glass fragmentation due to enhanced explosivity (Fisher and Schmincke, 1984). This lithofacies also occurs in Units IV and V.

Unit III also contains one distinctive interval (1.91 cm thick) with deformed tuffaceous mudstone intraclasts (up to ~20 cm in size) and clasts of scoria and pumice (up to 5 cm) supported in a deformed tuffaceous mudstone matrix; this is interpreted to represent a disaggregated slump or submarine debris flow deposit.

Lithostratigraphic Unit IV (1017.88 – 1120.11 mbsf)

Unit IV is ~6.2- 7.5 Ma in age (Figure 9), and is 102.23 m thick (Figure 10). It contrasts with the tuffaceous mudstone–dominated Units III and V, and consists of four lithofacies, in order of abundance: (1) normally–graded polymictic lapilli-tuff and

lapillistone (Figure 14). Lapilli are small (average 3-5 mm), and volcanic lithic clasts dominate over pumice, and are plagioclase-pyroxene andesites (Figure 14), that is, they are evolved. Shell fragments are also present, indicating that at least some of the material was sourced from shallow water. (2) intercalated white to gray-green evolved tuff, identical to that in Unit III (compare Figure 14C- with Figure 13B). Similarly, it forms multi-meter thick, non-bioturbated intervals with planar lamination or soft-sediment deformation. (3) dark gray evolved tuff, like that described in Units I, II and III, with plagioclase, pyroxene and pumice. (4) tuffaceous mudstone, like that described in Units I, II and III. For interpretation of the second through fourth lithofacies, see above. The first lithofacies (polymictic, evolved lapilli-tuff and lapillistone) occurs as very thick (multimeter) relatively well-sorted intervals with no internal stratification, composed of volcanic clasts of a variety of evolved types (Figures14A, 14B). These characteristics suggest deposition from high-concentration density currents, probably by mass wasting or resedimentation from one or more volcanoes; alternatively, this facies could be products from pyroclastic eruptions that mobilized large volumes of lithic clasts. This lithofacies is also abundant in Unit V.

Lithostratigraphic Unit V 1120.11 to 1320.00 mbsf)

Lithostratigraphic Unit V is ~7.5 – 9 Ma in age (Figure 9), and is 199.89 m thick (Figure 10). It is distinguished largely on the basis of its intervals of monomictic reversely graded pumice lapilli-tuff (Figure 15A); these distinctive beds, with their flattened pumice and nonflattened pumice dispersed in a tuff matrix, contrast with the polymictic, dominantly lithic lapilli-tuff of the overlying and underlying units (IV and

VI). The flattened pumice is referred to as "fiamme" with no connotation of welding compaction; in fact most or all of the pumices were probably flattened during diagenesis. Each monomictic reversely graded pumice lapilli-tuff in Unit V has (Figure 15A): (1) a sharp base, typically eroded into the underlying tuffaceous mudstone, overlain by (2) evolved tuff with abundant glass shards and grains of pumice, in turn grading upward into (3) pumice lapilli-tuff with flattened or non-flattened pumices that become progressively coarser upward (i.e., reversely graded); this passes upward into (4) tuffaceous mudstone. This lithofacies is thus composed almost entirely of vitric material (glass shards and pumice). This monomictic tuff with pumice and fiamme makes up 13% of Unit V and recurs throughout. We interpret this lithofacies to represent density current deposits, based on (a) basal scours; (b) poor sorting with ash-sized material with pumice lapilli or fiamme that become more abundant upward in each bed, indicating density grading; and (c) the increase in tuffaceous mudstone at the top of each bed. The monomict composition and the presence of abundant evolved glass shards, pumice, and broken crystals indicate that these were fed from pyroclastic eruptions.

Similar to Units I, III, and IV, Unit V also has tuffaceous mudstone (69%); evolved tuff (15%), some with soft-sediment faulting (Figure 15B); and lapilli-tuff and lapillistone (3%) with lithic and volcanic rock fragments (Figure 15C).

Lithostratigraphic Unit VI (1320.00 to 1459.80 mbsf)

Lithostratigraphic Unit VI is older than ~9 Ma (Figure 9) and extends to at least 10.97-11.85 Ma in age, and is 139.80 m thick (Figure 10). It is characterized by an abundance of polymictic lapilli-tuff with pumice and lithic clasts (Figure 16A, 16B), although it also

505 contains monomictic pumice lapilli-tuff (Figures 16C, 16D). The top of lithostratigraphic
506 Unit VI is marked by the first appearance of multiple intervals of polymictic lapilli-tuff,
507 and its base is marked by the top of a very distinctive black monomictic glassy
508 lapillistone and lapilli-tuff in the upper part of Unit VII.

509 The polymictic lapilli-tuff and lapillistone forms very thick beds (>1.5 m, the length of
510 a core section, or up to 2.8 m thick assuming complete recovery between core sections).
511 Tuff and tuffaceous mudstone intervals are interbedded. Polymictic lapilli-tuff with
512 pumice and lithic clasts is four times more abundant than monomictic pumice lapilli-tuff
513 in Unit VI; monomictic varieties contain only pumice, whereas polymictic varieties have
514 evolved and lesser mafic volcanic lithic clast types as well as pumice clasts (Figures 16A,
515 16B). The polymictic lapilli-tuff with lithic clasts and pumice shows a complete
516 gradation from clast-supported (Figure 16E), to matrix-supported (Figure 16F) whereas
517 the monomictic pumice lapilli-tuff is entirely matrix-supported.

518 Lithic lapilli in Unit VI are dominantly:

519 • Porphyritic andesite with plagioclase and clinopyroxene (Figures 16G, 16H, 16I,).
520 Clasts of this type also occur as scattered small blocks (>6.4 cm in size) in the polymictic
521 lapilli-tuff.

522 • Rhyolite-dacite, which becomes more common near the rhyolite intrusive sheet with
523 peperitic boundaries, described as igneous Unit 1 below. These include crystal-poor and
524 porphyritic varieties, with amphibole, plagioclase, and quartz.

525 Pumice lapilli clasts in Unit VI are light to dark green and commonly flattened by
526 compaction and lithification into fiamme (Figures 16C, 16D). Red to brown tuffaceous
527 mudstone clasts are also present in Unit VI (Figure 16B).

In summary, Unit VI is dominated by lapilli-tuff and lapillistone in very thick (multimeter) beds with no internal stratification, composed of volcanic clasts of a variety of evolved types (Figures 16A, 16B); this was deposited from high-concentration density currents, probably by mass wasting or resedimentation from one or more volcanoes. Additionally, Unit VI has matrix-supported monomictic pumice lapilli tuff that may have had been fed from pyroclastic eruptions.

Igneous Unit 1 (1388.86 to 1390.07 mbsf)

The only igneous unit at Site U1437 consists of a single rhyolite intrusion, which lies within lithostratigraphic Unit VI (Figure 10). As noted above, igneous Unit 1 yielded a U-Pb zircon age of 13.6 Ma ±1.7 in shore-based work immediately following the expedition, described by Konrad et al. (2016). Core recovery is much lower in igneous Unit 1 (~45%) than its host volcaniclastic rock (~94%), and the recovered igneous Unit 1 core material is fractured by drilling disturbance (Figure 17), probably due to greater competency of the rhyolite intrusion compared to the surrounding volcaniclastic host. Therefore, although only 1.21 m thickness was described for igneous Unit 1 (Figure 17), its maximum thickness is estimated at 6.50 m assuming all the material not recovered from this interval was part of igneous Unit 1.

Shipboard geochemical analysis (discussed below) shows that igneous Unit 1 is a rhyolite with 74.5% SiO_2. It has sieve-textured subhedral plagioclase (up to 4 mm, ~7%), euhedral hornblende (up to 0.5 mm, ~3%), large anhedral to subhedral quartz (up to 8 mm, ~1%) with fresh glassy melt inclusions, some opaque minerals, and rare zircon (<30 μm in size). Flow banding is observed across the entire unit in various orientations

(Figure 17B). The groundmass varies from cryptocrystalline near the upper and lower contacts to fine grained in the center of the unit (Figure 17B). Paleomagnetic data on igneous Unit 1 show a consistent, single component demagnetization and normal polarity with appropriate inclination of the characteristic remanent magnetization, supporting the interpretation that igneous Unit 1 is an intrusion, rather than simply a large clast. The upper margin of the intrusion is chilled, and the overlying lapilli-tuff is baked (Figure 17B), also indicating that igneous Unit 1 is an intrusion rather than a clast or lava. The lower contact of igneous Unit 1 is peperitic, defined as a magma-wet sediment mixture (Busby-Spera and White, 1987); the contact shows complex mingling between the intrusion and the host, including crenulated lobate margins on the intrusion and dispersal of the magma into the host on the microscopic scale (Figure 17C). Peperite is considered penecontemporaneous with the section it intrudes (Busby-Spera and White, 1987). Blocks of similar material occur in the host, Unit VI (rhyolite-dacite blocks, described above), indicating that the body locally vented onto the surface during accumulation of Unit VI.

Lithostratigraphic Unit VII (1459.80 to 1806.50 mbsf)

Unit VII is older than 10.97 – 11.85 Ma and is 346.70 m thick (Figure 10). It is ~90% extremely thick bedded, nongraded, nonstratified, poorly sorted, coarse-grained angular andesitic lapilli-tuff, in places with blocks tens of centimeters in size (Figure 18). Some of these blocks have quenched margins, jigsaw-fit textures, intricate fluidal margins, or peperitic margins, described in detail below. These features indicate that the blocks were emplaced hot, so the blocks could have originated as hot clasts, lava, and/or

574 intrusions. Thus Unit VII is interpreted to be a near-vent deposit. Unit VII is divided into
575 upper and lower parts (shallower and deeper than 1643.73 mbsf).

576 *Upper Part of Unit VII: Black glassy lapillistone and lapilli-tuff*

577 The upper part of Unit VII consists of one massive (nonstratified) ~184-m thick
578 deposit of homogeneous, nonvesicular glassy black lapillistone and lapilli-tuff. The glass
579 clasts are unaltered and angular, with abundant large clinopyroxene glomerocrysts and
580 plagioclase glomerocrysts (Figure 18A). The glass is isotropic and nonvesicular, and
581 bubble-wall shards or broken crystals are absent (Figures 18B, 18C). Only a few volcanic
582 lithic clasts are present, some with quenched margins, and a few red oxidized clasts also
583 occur. The black glassy lapillistone and lapilli-tuff lithofacies lacks stratification
584 completely, except for one thin (~25 cm thick) interval of crudely stratified ash. The
585 angular, glassy, nonvesicular, monomict character of the clasts, together with the lack of
586 bubble-wall shard or broken crystals, indicates fragmentation by autobrecciation and
587 quenching of lava in a submarine environment (i.e., hyaloclastite). The few nonglassy
588 clasts in the deposit suggest minor accidental incorporation of clasts during transport, but
589 most of the unit is monomictic and nonstratified, indicating minimal resedimentation. A
590 lack of tuffaceous mudstone interbeds indicates rapid accumulation.

591 *Lower Part of Unit VII: Coarse-grained massive lapilli-tuff with in situ quench-*
592 *fragmented blocks*

593 The lower part of Unit VII (~157 m thick) is dominated by a lithofacies of green
594 (i.e., altered) angular andesite lithic lapilli-tuff, in places with blocks up to 53 cm in size
595 (tuff breccia) (see Figures 18F, 18G). Like the black glassy lapillistone and lapilli-tuff

596 unit that forms the upper part of lithostratigraphic Unit VII, these lithic lapilli-tuff and
597 tuff-breccia intervals are massive, forming extremely thick intervals of nonstratified, very
598 poorly sorted monomictic andesite lapilli-tuff with blocks, but unlike the upper part of
599 Unit VII, the lower part has intercalated stratified lithic lapilli-tuff and tuff (also altered
600 green). Clasts in the extremely thick nonstratified intervals are angular or have very
601 irregular shapes, including jig-saw fit clasts (Figures 18D, 18E), indicating very minimal
602 transport. Many intervals contain glassy blocks and coarse lapilli, and some have glassy
603 rims and poorly inflated breadcrust or cauliflower texture, indicating that clasts came to
604 rest at high temperatures (Figures 18F, 18G). In at least one case, a clast appears to be
605 surrounded by sediment with a baked margin. Additionally, there are no clasts with
606 broken chilled margins as would be expected if the clasts were transported and deposited
607 after they cooled. In some intervals, very angular, jigsaw-fit hyaloclasts (formed of
608 quenched glass) indicate in situ mixing of hot clasts and/or intrusions with the host
609 hyaloclastic tuff-breccia, all of the same andesitic composition. On the basis of the core,
610 it is not possible to determine whether all of these features formed on hot clasts or if
611 some of these features formed on the complexly embayed margins of small intrusive
612 bodies or lava. Further support of hot emplacement is provided by paleomagnetic
613 inclinations from two of the clasts; despite multidomain overprinting, the
614 demagnetization analyses of these two individual clasts resolved the characteristic
615 reversed polarity expected for hot emplacement (for more details see Tamura et al.,
616 2015a). Some intervals have more heterogenerous andesite lithic clast types, with
617 variable plagioclase and pyroxene contents, and ranging from nonvesicular to moderately
618 vesicular, indicating resedimentation.

Petrophysical data from cores and downhole logging

We collected petrophysical data from all cores, including density and porosity, sonic velocity, magnetic susceptibility and natural gamma radiation (Figure 19). In addition, we conducted downhole logging operations in Hole U1437D, from 92 to ~960 mbsf. The logging parameters included those measured on Figure 19, plus bulk resistivity, and micro-resistivity imaging (not presented here). The top 92 m could not be logged because the drill pipe extended to that depth for operational and safety reasons. The logs extend to ~960 mbsf because 980 mbsf was the depth of the hole when the drill string had to be retrieved for a bit change and it seemed prudent to conduct a first set of downhole measurements at that time. After logging was completed, Hole U1437D was deepened from 980 to 1105 mbsf, where drilling difficulties were encountered and the hole had to be terminated. We drilled a new Hole U1437E to that depth without coring, deployed a 1086-m long casing string, and cored from 1104 to 1806 mbsf. At that time a technical problem precluded re-entry and we could not log Hole 1437E. Fortunately the onboard petrophysical measurements were unaffected (Figure 19). The two shallowest logging unit boundaries, between 1 and 2 and between 2 and 3, correspond to the lower boundaries of sharp resistivity anomalies at 310 m and 612 m, respectively, and both lie within lithologic Unit I. Logging unit boundary 3 to 4 corresponds to lithologic unit boundary I/II at 680 m. The lower boundary of the conspicuous lithologic Unit II was not defined in the logging data, although it can be clearly recognized in the resistivity log. The deepest logging unit boundary 4/5 at 789 m corresponds to an increase in natural gamma radiation and resistivity and lies within lithologic Unit III (Figure 19).

642 The first order trends in physical properties are indicated by density, porosity,
643 resistivity and p-wave velocity. These all change rapidly with depth in the interval ~700-
644 950 mbsf, which corresponds to lithologic Unit II and most of Unit III. The trends above
645 and below this interval have similar and lower rates of change with depth; the range of
646 values is significantly larger below 950 mbsf.

647 The higher rate of downhole increase in density and sonic velocity, and the
648 corresponding decrease in porosity, in the interval 700-950 mbsf, are the result of
649 compaction and cementation by incipient diagenesis in the volcaniclastics and tuffaceous
650 mudstone of lithologic Units II and III. These trends are accompanied by significant
651 changes in the magnetic susceptibility (MS) and natural gamma radiation (NGR), which
652 are compositional proxies. MS is low in the upper 700 m at Site U1437, increases two to
653 threefold in the interval 700-950 mbsf, and below 950 mbsf shows a cyclic pattern with
654 values ranging from lowest to highest in the entire section. MS variations most likely
655 reflect oxide concentration, particularly magnetite. NGR, in contrast, has generally higher
656 values above 1000 mbsf and lower values below, suggesting first-order changes in
657 sediment provenance above and below that depth; this lies at the Unit III/IV boundary at
658 ~6.2 Ma (Figure 19).

659 The interval at 290-312 mbsf (logging depth, within Unit I, Figure 19) shows a
660 sharp resistivity increase to twice the local baseline value. In the Formation
661 MicroScanner (FMS) micro-resistivity images, this interval appears slightly less layered
662 (more granular or chaotic?) than the overlying and underlying intervals. In this same
663 high-resistivity interval, MS values triple, and natural gamma radiation drops to local
664 minimum values. The corresponding interval in the cores (at coring depth scale) had

665 almost no recovery: Core U1437B-40X (291.1-300.8 mbsf) had 1.8 m recovery (12%)
666 and the recovered tuffaceous mud and ash layers are indistinguishable from overlying
667 sediments. Cored intervals 41-42X (300.8-320.2 mbsf) had zero recovery. Furthermore,
668 when we attempted to drill Hole U1437C to 425 mbsf without coring, circulation and
669 rotation were lost at 309.7 mbsf. The bit had to be dropped and the stuck pipe had to be
670 worked for several hours before it became free and could be retrieved, at which point
671 Hole U1437C was abandoned. The drilling problems in this interval suggests loose or
672 fractured material, however, that would not explain higher resistivity, which may indicate
673 less porosity (cementation, remolding) or less saline pore water. The high-resistivity
674 interval corresponds to the sequence boundary between seismic layers L2 and L3 (Figure
675 8), a boundary that may reflect a period of non-deposition, erosion and/or deposition by
676 mass wasting, and/or lateral fluid flow. The MS and NGR signals could indicate a
677 primary compositional change or alteration associated with fluid flow. At this time we
678 simply don't know what this mystery interval represents. An interval with similar log
679 signature at 607.3-614.6 m (logging depth) has also lower, but reasonably good core
680 recovery (~60%, compared to ~82% in 50 m above and ~97% in 50 m below). The
681 recovered material from this interval is tuffaceous mudstone with intercalations of tuff
682 and shows no obvious characteristics that would differentiate it macroscopically from the
683 overlying and underling intervals.

684 Over the entire section at Site U1437, both MS and NGR records show high-
685 amplitude variations at the decimeter to meter depth scale that can be linked to lithologic
686 and compositional changes. These relationships cannot be elaborated or illustrated within
687 the scope of this overview and are subject to ongoing studies.

688

689 **Interpretation of Depositional Environment at Site U1437: Deepwater Basinal**
690 **Succession**

691 As noted above, the section drilled at Site U1437 accumulated in a deepwater volcano-
692 bounded basin between the Manji and Enpo seamount chains. We now present evidence
693 that the section is best described as a deepwater basinal succession, characterized by fine-
694 grained well-stratified, laterally continuous deposits in the upper 75% of the section; this
695 passes downward into proximal volcaniclastic deposits in the lower 25% of the section,
696 which we infer records eruption and sedimentation from nearby volcanoes and localized
697 venting within the deepwater basinal setting.

698

699 Upper 75% of the section drilled at Site U1437

700 This part of the section (Units I through V; 0–1320 mbsf; ca. 0-7.5 Ma) has the
701 following characteristics:

702 • It is mostly tuffaceous mudstone (~60%) deposited from hemipelagic rain, dilute turbid
703 flows, bottom currents/sediment drift, or some combination thereof.

704 • The grain size of volcanic clasts in the discrete volcaniclastic layers is small: about half
705 ash and half fine-grained lapilli.

706 • Lack of block-sized clasts.

707 • Little evidence for density current deposits, except in Unit II, which is thin; most of the
708 volcaniclastics could represent suspension fallout from distal eruptions.

709 • There is no geomorphic or seismic stratigraphic evidence for fan- or wedge-shaped
710 sediment bodies or of chaotic facies; instead, the seismic reflection images show laterally

711 persistent tabular stratification, consistent with the fine grained character of the section
712 drilled.

713 In summary, from 0 Ma to ca. 7.5 Ma, hemipelagic sedimentation dominated the
714 basin, with ash regularly deposited in the area and variably mixed with mud of uncertain
715 origin (possible origins of the mud discussed below). Lapilli-sized fragments (albeit fine-
716 grained) were only provided to the basin in one brief episode at 4.3 Ma, represented by
717 Unit II, and it is dominated by evolved pumice lapilli indicative of an explosive volcanic
718 event; however the fine grain size of the lapilli could indicate that the eruption was
719 relatively distal, and this unit only represents 3% of the drilled section. Two aspects of
720 the upper 75% of the section are difficult to explain: (1) The section is much more mud-
721 rich than expected for an arc-proximal sedimentary succession, and (2) the grain size of
722 the volcaniclastics is much smaller than expected for an intra-arc basin surrounded by
723 volcanoes.

724

725 Lower 25% of the section drilled at Site U1437

726 This part of the section (Unit VI, igneous Unit 1, and Unit VII; 1320-1804 mbsf; ca. 9
727 -14 Ma) differs from the upper 75% in the following ways:

728 • Tuffaceous mudstone is minor (10% of Unit VI) to absent (Unit VII).

729 • The grain size of volcanic clasts increases dramatically, with coarse-grained lapilli
730 dominating the section, and blocks occurring in Unit VII.

731 • Lapilli-sized volcaniclastics of unit VI are polymictic and formed thick massive beds,
732 some graded; these were deposited from density currents carrying detritus from

seamounts surrounding the Enpo-Manji Basin. Intervening minor tuffaceous mudstone record background hemipelagic sedimentation between density current events.

• Andesite lapilli tuff and tuff breccia of Unit VII are monomictic, and show macroscopic textural evidence of quench fragmentation and paleomagnetic evidence of emplacement at high temperatures. The absence of background sediment (tuffaceous mudstone) indicates high/steady volcanic input. Unit VII is a vent-proximal deposit.

• Unit VI was intruded by a quartz-phyric rhyolite-dacite sheet dated at 13.6 +1.6/–1.7 Ma (igneous Unit 1); this intrusion is a peperite (formed by mixing of magma and wet sediment), indicating that it formed contemporaneously with the section it intrudes; furthermore, blocks of igneous Unit I are scattered through the section above and below, indicating its contemporaneity with Unit VI.

In summary, from ~9 to 14 Ma, coarse-grained volcaniclastic sedimentation dominated the area of Site U1437, with polymictic material derived from adjacent volcanoes (Unit VI), and monomictic material produced by local eruptions (Unit VII) and peperite intrusions (igneous Unit 1), with little to no evidence for resedimentation, i.e., dominantly in situ.

Shipboard Igneous Geochemistry

This section is brief, because shore-based micro-analytical igneous geochemical studies (in progress) are expected to be much more revealing than the ship-based studies. This is because:

• The fine grain size of the upper 75% of the section largely precluded analysis of individual clasts by shipboard techniques, requiring us to analyze bulk samples, referred

to as “volcaniclastic samples” (Figures 20, 21), taken from different parts of lapilli-tuff or tuff beds, some of which are graded. Shipboard analyses of individual clasts are restricted to: (1) a single dacite pumice clast from Unit II, (2) a single andesitic lithic clast from Unit IV. These two clasts, along with igneous Unit I, are referred to as “igneous samples”. Shore-based microanalytical techniques will allow analysis of individual clasts that are lapilli- to ash-sized.

• Due to alteration, shipboard analyses relied largely on Zr, Zr/Y and and Zr/Y vs. SiO_2 plots for distinguishing defining geochemical units (Figures 20, 21). We focused on Zr and Y because they are relatively fluid immobile and remain robust during alteration (Gill et al., 1994). We used shipboard Zr/Y analyses as an indicator for magmatic provenance and to distinguish between rear-arc and arc-front sources. Micro-analytical techniques will be more successful at exploiting relict glass domains, and will be used to determine the chemistry of minerals, which are less altered than the glass.

Downhole geochemical variations in Units I–V generally reflect the relative proportions of distal arc-front and proximal rear-arc volcanic sources (Figure 21). As a general trend, coarse-grained volcaniclastics from Units II and IV show stronger rear-arc affinity compared to fine-grained tuff from Units I, III, and V. Complications for provenance arise from mixing evident by mafic and evolved glass shards in fine-grained volcaniclastic samples. Also, alteration is pervasive in Units III and V. The predominance of ash layers from Unit I containing low K2O relative to SiO2 indicates a likely arc front or active rift (<1s Ma) provenance. Volcaniclastics in Unit I with high Zr/Y could be mixtures of mafic ash from arc front basalt-dominated island volcanoes, and evolved ash from the rhyolite-dominated submarine calderas (R2 rhyolites), which have high Zr/Y;

779 however, this cannot be confirmed without onshore in situ analyses of glass. The coarse-
780 grained deposits from Units II and IV indicate proximal sources. Active Manji seamount
781 chain volcanoes around the time of deposition of Unit II (4.2–4.3 Ma) were the Meireki
782 Seamount (3.76 Ma; Ishizuka et al., 1998) ~20 km to the north and the Daigo-Nishi-
783 Aogashima Knoll (5.05 Ma; Ishizuka et al., 2003b) ~40 km to the northeast of Site
784 U1437 (Figure 7). Both are rhyolite volcanoes with similar SiO2 contents (72–76 wt%),
785 whereas Meireki Seamount volcanic rocks have higher K2O (~3 wt%) but lower Zr/Y
786 (~2.8) compared to the Daigo-Nishi-Aogashima Knoll (K2O = ~1.5 wt%; Zr/Y = ~4.4)
787 (Hochstaedter et al., 2001). Although the limited data (5 analyses in total) available for
788 both seamounts preclude reliable geochemical matching with Unit II volcaniclastics, they
789 are potential sources for lapilli in Unit II considering their geographic locations, ages, and
790 chemical composition. Similarly, single clast compositions of Unit IV can be tentatively
791 matched to available data for Manji Seamount volcanic rocks (Figure 7; ~6.5–6.9 Ma;
792 Ishizuka et al., 2002). Two high-K2O volcaniclastics resemble the high-K Manji
793 Seamount rocks with potassic alteration, whereas most volcaniclastics from Unit IV
794 follow the trend for altered Manji Seamount rocks (Ishizuka et al., 2002), including
795 depletions in CaO with increasing SiO2 (see Figure F44 of Tamura et al., 2015a). Unit V
796 is primarily tuffaceous mudstone, and given the pervasive alteration throughout this unit,
797 it is difficult to provide an accurate provenance for its volcaniclastic intervals.

798 The geochemistry of samples from Units VI and VII and igneous Unit 1 does not
799 fall neatly into the rear-arc field, but instead spans both fields (Figure 20), even though a
800 rear-arc source is demanded by the vent-proximal nature of the deposits (described
801 above). One of the goals of Expedition 350 (Tamura et al., 2013) was to determine the

802 timing of development of geochemical asymmetry between the arc front and rear arc.
803 This is important because dredge samples that were already in hand from Neogene
804 volcanoes of the rear arc were more "continental" in chemical composition than dredge
805 and drill core samples from the arc front, therefore making the rear arc more suitable as a
806 possible building block for continental crust. We presented two models for the
807 development of arc asymmetry: "from the beginning" and "from the middle" (Tamura et
808 al., 2013). The "from the beginning" hypothesis stipulated that arc asymmetry was
809 established at Eocene arc inception and persisted through the Neogene. The "from the
810 middle" hypothesis stipulated that the asymmetry developed during an arc hiatus
811 associated with opening of the Shikoku backarc basin at 27-17 Ma. On the basis of
812 seismic stratigraphy, we expected to reach Oligocene (>23 Ma) strata at 1250 mbsf, to
813 determine which hypothesis was correct, but instead those strata are 9 Ma (Late Miocene;
814 lower part of Unit V), so the chemistry of the Paleogene rear arc remains unknown.
815 However, the compositional heterogeneity of Units VI and VII suggests that arc
816 asymmetry did not develop until after ~13 Ma (Middle Miocene), which is *during* the
817 Neogene, that is, neither "from the beginning" nor "from the middle".
818
819 **Depositional Model**
820 The biggest surprise of the expedition was the predominance of tuffaceous mud and
821 the fine grain size of the volcaniclastics at Site U1437. We expected to drill into a
822 volcaniclastic apron (see Scientific Prospectus; Tamura et al., 2013), with abundant large
823 lapilli- to block-sized volcanic clasts that could be geochemically analyzed individually
824 on the ship. This is not what we encountered, but before presenting the depositional

825 model, it is necessary to define the term "volcaniclastic apron" in order to show how the
826 depositional model for Site U1437 differs from models for volcaniclastic aprons.

827 Although some may use the term "volcaniclastic apron" to loosely refer to any
828 accumulation of sediment around a volcano or chain of volcanoes, the term has been used
829 in a much more rigorous sense by sedimentologists over the past 40 years (Karig and
830 Moore, 1975b; Sample and Karig, 1982; Carey and Sigurdsson, 1984; Farquharson et al.,
831 1984; Fisher, 1984; Busby-Spera, 1985, 1988; Cas and Wright, 1987; Smith, 1987; White
832 and Busby-Spera, 1987; Houghton and Landis, 1989; Palmer and Walton, 1990; Fisher
833 and Smith, 1991; Fisher and Schmincke, 1994; Smith and Landis, 1995; Orton, 1996;
834 Wright, 1996; Mitchell, 2000; Carey, 2000; Gamberi, 2001; Karátson and Németh, 2001;
835 Allen et al., 2006; Casalbore et al., 2010; Carey and Schneider, 2011). In these papers, a
836 volcaniclastic apron is defined as a thick accumulation of coarse volcanic debris that
837 fringes a volcano or a chain of volcanoes and builds outward from them; volcaniclastic
838 aprons are typically fan shaped or are composed of coalescing fans that form a wedge.
839 They are steep in their proximal reaches, with abundant large lithic blocks and slumps,
840 passing smoothly into medial to distal reaches that have gentler slopes, formed of debris
841 flow and coarse-grained pyroclastic density current deposits. For example, the "volcanic
842 apron" of Gran Canaria (Shipboard Scientific Party, 1995) is a volcaniclastic apron
843 (Funck et al., 1996), consisting of volcano-flank seismically chaotic pillow breccia and
844 hylaoclastite and poorly stratified debris flow deposits, which pass basinward into
845 crudely stratified slump, debris flow, and turbidity current deposits. The submarine flanks
846 of Anahatan Volcano and Northeast Anahatan Volcano (Mariana Arc) are largely
847 mantled with volcaniclastic aprons, which extend 5-20 km from the island of Anahatan;

848 these have slopes decreasing from 15-25° to 5° with distance, and their outer edge is
849 marked by a distinct break in slope, with abyssal sediment beyond (Chadwick et al.,
850 2005). Volcaniclastic aprons form in both nonmarine and marine environments, and they
851 commonly prograde into basins with time, producing an overall upward-coarsening
852 sequence.

853 The depositional model for Site U1437 must take account of the fact that it is an
854 entirely deepwater deposit, and using the criteria above, it clearly does not represent a
855 volcaniclastic apron. The depositional model may instead be based on analogies with the
856 other major type of deepwater depositional system, the submarine fans and aprons of
857 siliciclastic deepwater systems. Submarine fans and aprons are relatively coarse grained
858 constructional features, whereas the basin plain beyond is flat and fine grained with
859 laterally continuous deposits (Reading and Richards, 1994; Stow et al., 1996; Richards,
860 2009). The upper 75% of the section drilled at Site U1437 is analogous to the basin plain;
861 it is a fine-grained, well-stratified sequence with laterally continuous layers. For this
862 reason we refer to it as a deepwater basinal succession, not a volcaniclastic apron.

863 The lower 25% of the section, in contrast, consists largely of blocky hyaloclastic
864 deposits (Unit VII, 347 m) that cooled in situ with very limited remobilization and thus
865 represent near-vent deposits. It also includes lesser polymict lapilli tuffs (Unit VI, 140 m)
866 sourced from nearby volcanoes but also with rhyolite blocks locally derived from igneous
867 Unit 1 (within Unit VI). Therefore, the lower 25% of the section is dominated by
868 localized vent-related deposits within the deepwater basinal succession. As discussed
869 above, the geochemistry of the lower 25% also differs from the upper 75% of the section.
870

CONCLUSION: SURPRISES, AND QUESTIONS TO BE ADDRESSED IN SHORE-BASED INVESTIGATIONS

Four surprises resulted from drilling at U1437 that led to questions for ongoing (shore-based) investigation, to be summarized in future papers.

The first surprise is that the section is much more mud-rich than expected for an arc-proximal sedimentary succession. The section as a whole is 60% tuffaceous mudstone, with 89% in the uppermost 433 m, and with high sedimentation rates of 100-260 m/my for the upper 1300 m. What was the source of all that mud, and how was it deposited?

The second surprise is that the grain size of the volcaniclastics is much smaller than expected for an arc-proximal sedimentary succession, composed of half ash/tuff and half fine-grained lapilli tuff. No volcanic blocks are present in the upper 75% of the section. Yet Site U1437 lies downslope, within kms to tens of km, of seamounts dated at 6.86 – 6.53 (Manji), 3.76 Ma (Meoreki) and 5.05 Ma and 0.55 Ma (Daigo-Nishi-Aogashima Knoll) from dredged samples, as shown on Figure 7. This may indicate that most <7 Ma eruptions from the seamounts were small-volume effusions that did not produce much volcaniclastic material. Alternatively, the dredged samples represent late-stage, small volume eruptions that mantle the surfaces on the seamounts, and they were largely built before ~9 Ma.

The third surprise is that the section is much younger than predicted from seismic stratigraphy. For example, Oligocene (>23 Ma) strata were predicted at 1250 mbsf, but instead those strata are 9 Ma (Miocene).

Fourth, it was predicted that compositional divergence between arc-front and rear-arc magmas developed during a volcanic hiatus associated with opening of the backarc basin at 27-17 Ma, if it did not already exist from the time of arc inception in the Eocene (~45 Ma); however, preliminary data presented here suggest that this divergence only fully developed after ~13-14 Ma (Middle Miocene). The cause is not known.

ACKNOWLEDGEMENTS

We thank all of the personnel aboard the R/V *Joides Resolution* during Expedition 350 for their skill and dedication. The editorial staff at the IODP *JOIDES Resolution* Science Operator in TAMU are thanked for help with publication of the Expedition 350 Proceedings volume, which is summarized herein. We also thank Bob Stern for his participation as a shore-based scientist, and for encouraging us to write this paper.

Helpful reviews provided by two anonymous reviewers are gratefully acknowledged.

REFERENCES

Allen, S.R., Hayward, B.W., and Mathews, E., 2006. A facies model for a submarine volcaniclastic apron: the Miocene Manukau Subgroup, New Zealand. *Geological Society of America Bulletin,* 119(5–6):725–742. **http://dx.doi.org/10.1130/B26066.1**

Andrews, G.D.M., Schmitt, A.K., Busby, C.J. and Brown, S.R., 2015, Geochronology and geochemistry of zircons from IODP Site U1437 in the rear arc of the Izu-Bonin volcanic chain: American Geophysical Union (abstr).

Arculus, R., Ishizuka, O., and Bogus, K.A., 2013. Izu-Bonin-Mariana arc origins: continental crust formation at intraoceanic arc: foundations, inceptions, and early evolution. *International Ocean Discovery Program Scientific Prospectus,* 351. http://dx.doi.org/10.2204/iodp.sp.351.2013

Arculus, R., Ishizuka, O., Bogus, M.H. and the Expedition 351 Scientists, 2015, Proceedings of the Internaitonal Ocean Discovery Program Volume 351 publications .iodp.org. doi:10.14379/iodp.proc.351.101.2015

Bandy, W.L., and Hilde, T.W.C., 1983. Structural features of the Bonin arc: implications for its tectonic history. *Tectonophysics,* 99(2–4):331–353. **http://dx.doi.org/10.1016/0040-1951(83)90111-7**

Bloomer, S.H., Taylor, B., MacLeod, C.J., Stern, R.J., Fryer, P., Hawkins, J.W., and Johnson, L., 1995. Early arc volcanism and the ophiolite problem: a perspective from drilling in the western Pacific. *In* Taylor, B., and Natland, J. (Eds.), *Active Margins and Marginal Basins of the Western Pacific*. Geophysical Monograph, 88:1–30. **http://dx.doi.org/10.1029/GM088p0001**

Bryant, C.J., Arculus, R.J., and Eggins, S.M., 2003. The geochemical evolution of the Izu-Bonin arc system: a perspective from tephras recovered by deep-sea drilling. *Geochemistry, Geophysics, Geosystems,* 4(11):1094. **http://dx.doi.org/10.1029/2002GC000427**

Busby-Spera, C.J., 1985. A sand-rich submarine fan in the lower Mesozoic Mineral King caldera complex, Sierra Nevada, California. *Journal of Sedimentary Research,* 55(3):376–391. **http://dx.doi.org/10.1306/212F86D9-2B24-11D7-8648000102C1865D**

Busby-Spera, C.J., 1988. Evolution of a middle Jurassic back-arc basin, Cedros Island, Baja California: evidence from a marine volcaniclastic apron. *Geological Society of America Bulletin,* 100(2):218–233. **http://dx.doi.org/10.1130/0016-7606(1988)100<0218:EOAMJB>2.3.CO;2**

Busby-Spera, C.J., and White, J.D.L., 1987. Variation in peperite textures associated with differing host-sediment properties. *Bulletin of Volcanology,* 49(6): 765–776. **http://dx.doi.org/10.1007/BF01079827**

Carey, S., 1997. Influence of convective sedimentation on the formation of widespread tephra fall layers in the deep sea. *Geology,* 25(9):839–842. **http://dx.doi.org/10.1130/0091-7613(1997)025<0839:IOCSOT>2.3.CO;2**

Carey, S., 2000. Volcaniclastic sedimentation around island arcs. *In* Sigurdsson, H., Houghton, B.F., McNutt, S.R., Rymer, H., and Stix, J. (Eds.), *Encyclopedia of Volcanoes:* San Diego (Academic Press), 627–642

Carey, S., and Sigurdsson, H., 1984. A model of volcanogenic sedimentation in marginal basins. *In* Kokelaar, B.P., and Howells, M.F. (Eds.), *Marginal Basin Geology: Volcanic and Associated Sedimentary and Tectonic Processes in Modern and Ancient Marginal Basins*. Geological Society Special Publication, 16(1):37–58. **http://dx.doi.org/10.1144/GSL.SP.1984.016.01.04**

967 Carey, S.N., and Schneider, J.-L., 2011. Volcaniclastic processes and deposits in the deep
968 sea. *In* Hüneke, H., and Mulder, T. (Eds.), *Developments in Sedimentology* (Vol. 63)*:*
969 *Deep-Sea Sediments:* Oxford (Elsevier), 457–515. **http://dx.doi.org/10.1016/B978-0-**
970 **444-53000-4.00007-X**
971
972 Cas, R.A.F., and Wright, J.V., 1987. *Volcanic Successions, Modern and Ancient: a*
973 *Geological Approach to Processes, Products and Successions:* London (Allen and
974 Unwin).
975
976 Casalbore, D., Romagnoli, C., Chiocci, F., and Frezza, V., 2010. Morpho-sedimentary
977 characteristics of the volcaniclastic apron around Stromboli volcano (Italy). *Marine*
978 *Geology,* 269(3–4):132–148. **http://dx.doi.org/10.1016/j.margeo.2010.01.004**
979
980 Chadwick, W.W., Embley, R.W., Johnsons, P.D., Merle, S.G., Ristau, S. and Bobbitt, A.,
981 2005, The submarine flank of Anatahan Volcano, commonwealth of the Northern
982 Mariana Islands: Journal of Volcanology and Geothermal Research, v. 146, p. 8-25
983
984 Chen, J., An, Z., Liu, L., Ji, J., Yang, J., and Chen, Y., 2001. Variations in chemical
985 compositions of the eolian dust in Chinese Loess Plateau over the past 2.5 Ma and
986 chemical weathering in the Asian inland. *Science in China Series D: Earth Sciences,*
987 44(5):403–413. **http://dx.doi.org/10.1007/BF02909779**
988
989 Cosca, M.A., Arculus, R.J., Pearce, J.A., and Mitchell, J.G., 1998. 40Ar/39Ar and K-Ar
990 geochronological age constraints for the inception and early evolution of the Izu-Bonin-
991 Mariana arc system. *Island Arc,* 7(3):579–595. **http://dx.doi.org/10.1111/j.1440-**
992 **1738.1998.00211.x**
993
994 Dickinson, W.R., and Hatherton, T., 1967. Andesitic volcanism and seismicity around the
995 Pacific. *Science,* 157(3790):801–803. **http://dx.doi.org/10.1126/science.157.3790.801**
996
997 Farquharson, G.W., Hamer, R.D., and Ineson, J.R., 1984. Proximal volcaniclastic
998 sedimentation in a Cretaceous back-arc apron, northern Antarctic Peninsula. *In* Kokelaar,
999 B.P., and Howells, M.F. (Eds.), *Marginal Basin Geology: Volcanic and Associated*
1000 *Sedimentary and Tectonic Processes in Modern and Ancient Marginal Basins*.
1001 Geological Society Special Publication, 16:219–229.
1002 **http://dx.doi.org/10.1144/GSL.SP.1984.016.01.17**
1003
1004 Fisher, R.V., 1984. Submarine volcaniclastic rocks. *In* Kokelaar, B.P., and Howells, M.F.
1005 (Eds.), *Marginal Basin Geology: Volcanic and Associated Sedimentary Processes in*
1006 *Modern and Ancient Basins*. Geological Society Special Publication, 16:5–27.
1007 **http://dx.doi.org/10.1144/GSL.SP.1984.016.01.02**
1008
1009 Fisher, R.V., and Schmincke, H.-U., 1984. *Pyroclastic Rocks:* Berlin (Springer-Verlag).
1010 **http://dx.doi.org/10.1007/978-3-642-74864-6**
1011
1012 Fisher, R.V., and Smith, G.A., 1991. Volcanism, tectonics and sedimentation. *In* Fisher,

R.V., and Smith, G.A. (Eds.), *Sedimentation in Volcanic Settings*. Special Publication—SEPM (Society for Sedimentary Geology), 45:1–5. **http://dx.doi.org/10.2110/pec.91.45.0001**

Fisher, R.V., and Schmincke, H.-U., 1994. Volcaniclastic sediment transport and deposition. *In* Pye, K. (Ed.), *Sediment Transport and Depositional Processes:* Oxford, UK (Blackwell Scientific Publishing), 351–388.

Funck, T., Dickmann, T., Rihm, R., Krastel, S., Lykke-Andersen, H., and Schmincke, H.-U., 1996. Reflection seismic investigations in the volcaniclastic apron of Gran Canaria and implications for its volcanic evolution. *Geophysical Journal International,* 125(2):519–536. **http://dx.doi.org/10.1111/j.1365-246X.1996.tb00015.x**

Gamberi, F., 2001. Volcanic facies associations in a modern volcaniclastic apron (Lipari and Vulcano offshore, Aeolian Island arc). *Bulletin of Volcanology,* 63(4):264–273. **http://dx.doi.org/10.1007/s004450100143**

Gill, J.B., 1981. *Minerals and Rocks* (Vol. 16): *Orogenic Andesites and Plate Tectonics:* Berlin (Springer-Verlag).**http://dx.doi.org/10.1007/978-3-642-68012-0**

Gill, J.B., Hiscott, R.N., and Vidal, P., 1994. Turbidite geochemistry and evolution of the Izu-Bonin arc and continents. *Lithos,* 33(1–3):135–168. **http://dx.doi.org/10.1016/0024-4937(94)90058-2**

Hochstaedter, A.G., Gill, J.B., Kusakabe, M., Newman, S., Pringle, M., Taylor, B., and Fryer, P., 1990a. Volcanism in the Sumisu Rift, I. Major element, volatile, and stable isotope geochemistry. *Earth and Planetary Science Letters,* 100(1–3):179–194. **http://dx.doi.org/10.1016/0012-821X(90)90184-Y**

Hochstaedter, A.G., Gill, J.B., and Morris, J.D., 1990b. Volcanism in the Sumisu Rift, II. Subduction and non-subduction related components. *Earth and Planetary Science Letters,* 100(1–3):195–209. **http://dx.doi.org/10.1016/0012-821X(90)90185-Z**

Hochstaedter, A.G., Gill, J.B., Taylor, B., Ishizuka, O., Yuasa, M., and Morita, S., 2000. Across-arc geochemical trends in the Izu-Bonin arc: constraints on source composition and mantle melting. *Journal of Geophysical Research: Solid Earth,* 105(B1):495–512. **http://dx.doi.org/10.1029/1999JB900125**

Hochstaedter, A., Gill, J., Peters, R., Broughton, P., Holden, P., and Taylor, B., 2001. Across-arc geochemical trends in the Izu-Bonin arc: contributions from the subducting slab. *Geochemistry, Geophysics, Geosystems,* 2(7):1019. **http://dx.doi.org/10.1029/2000GC000105**

Houghton, B.F., and Landis, C.A., 1989. Sedimentation and volcanism in a Permian arc-related basin, southern New Zealand. *Bulletin of Volcanology,* 51(6):433–450. **http://dx.doi.org/10.1007/BF01078810**

Ishizuka, O., Uto, K., Yuasa, M., and Hochstaedter, A.G., 1998. K-Ar ages from seamount chains in the back-arc region of the Izu-Ogasawara arc. *Island Arc,* 7(3):408–421.**http://dx.doi.org/10.1111/j.1440-1738.1998.00199.x**

Ishizuka, O., Yuasa, M., and Uto, K., 2002. Evidence of porphyry copper-type hydrothermal activity from a submerged remnant back-arc volcano of the Izu-Bonin arc: implications for the volcanotectonic history of back-arc seamounts. *Earth and Planetary Science Letters,* 198(3–4):381–399. **http://dx.doi.org/10.1016/S0012-821X(02)00515-0**

Ishizuka, O., Taylor, R.N., Milton, J.A., and Nesbitt, R.W., 2003a. Fluid-mantle interaction in an intraoceanic arc: constraints from high-precision Pb isotopes. *Earth and Planetary Science Letters,* 211(3–4):221–236. **http://dx.doi.org/10.1016/S0012-821X(03)00201-2**

Ishizuka, O., Uto, K., and Yuasa, M., 2003b. Volcanic history of the back-arc region of the Izu-Bonin (Ogasawara) arc. *In* Larter, R.D., and Leat, P.T. (Eds.), *Tectonic and Magmatic Processes*. Geological Society Special Publication, 219(1):187–205. **http://dx.doi.org/10.1144/GSL.SP.2003.219.01.09**

Ishizuka, O., Kimura, J.-I., Li, Y.B., Stern, R.J., Reagan, M.K., Taylor, R.N., Ohara, Y., Bloomer, S.H., Ishii, T., Hargrove, U.S., III, and Haraguchi, S., 2006a. Early stages in the evolution of Izu-Bonin arc volcanism: new age, chemical, and isotopic constraints. *Earth and Planetary Science Letters,* 250(1–2):385–401. **http://dx.doi.org/10.1016/j.epsl.2006.08.007**

Ishizuka, O., Taylor, R.N., Milton, J.A., Nesbitt, R.W., Yuasa, M., and Sakamoto, I., 2006b. Variation in the mantle sources of the northern Izu arc with time and space—constraints from high-precision Pb isotopes. *Journal of Volcanology and Geothermal Research,* 156(3–4):266–290. **http://dx.doi.org/10.1016/j.jvolgeores.2006.03.005**

Ishizuka, O., Taylor, R.N., Yuasa, M., and Ohara, Y., 2011. Making and breaking an island arc: a new perspective from the Oligocene Kyushu-Palau arc, Philippine Sea. *Geochemistry, Geophysics, Geosystems,* 12(5):Q05005. **http://dx.doi.org/10.1029/2010GC003440**

Karátson, D., and Németh, K., 2001. Lithofacies associations of an emerging volcaniclastic apron in a Miocene volcanic complex: an example from the Börzsöny Mountains, Hungary. *International Journal of Earth Sciences,* 90(4): 776–794.

Karig, D.E., and Moore, G.F., 1975a. Tectonic complexities in the Bonin arc system. *Tectonophysics,* 27(2):97–118. **http://dx.doi.org/10.1016/0040-1951(75)90101-8**

Karig, D.E., and Moore, G.F., 1975b. Tectonically controlled sedimentation in marginal basins. *Earth and Planetary Science Letters,* 26(2):233–238. **http://dx.doi.org/10.1016/0012-821X(75)90090-4**

Kodaira, S., Sato, T., Takahashi, N., Ito, A., Tamura, Y., Tatsumi, Y., and Kaneda, Y., 2007a. Seismological evidence for variable growth of crust along the Izu intraoceanic arc. *Journal of Geophysical Research: Solid Earth,* 112(B5):B05104. **http://dx.doi.org/10.1029/2006JB004593**

Kodaira, S., Sato, T., Takahashi, N., Miura, S., Tamura, Y., Tatsumi, Y., and Kaneda, Y., 2007b. New seismological constraints on growth of continental crust in the Izu-Bonin intra-oceanic arc. *Geology,* 35(11):1031–1034. **http://dx.doi.org/10.1130/G23901A.1**

Kodaira, S., Sato, T., Takahashi, N., Yamashita, M., No, T., and Kaneda, Y., 2008. Seismic imaging of a possible paleoarc in the Izu-Bonin intraoceanic arc and its implications for arc evolution processes. *Geochemistry, Geophysics, Geosystems,* 9(10):Q10X01. **http://dx.doi.org/10.1029/2008GC002073**

Konrad, K., Schmitt, A.K., Andrews, G.D., Horle, K., Brown, S.R., Koppers, A.A.P., Busby, C. and Tamura, Y., 2016, 40Ar/39Ar dating and zircon chronochemistry for the Izu-Bonin rear arc, IODP site U1437: American Geophysical Union Fall Meeting, Abstract V13C-2853.

Kuno, H., 1959. Origin of Cenozoic petrographic provinces of Japan and surrounding areas. *Bulletin of Volcanology,* 20(1):37–76. **http://dx.doi.org/10.1007/BF02596571**

Machida, S., and Ishii, T., 2003. Backarc volcanism along the en echelon seamounts: the Enpo Seamount chain in the northern Izu-Ogasawara arc. *Geochemistry, Geophysics, Geosystems,* 4(8):9006. **http://dx.doi.org/10.1029/2003GC000554**

Machida, S., Ishii, T., Kimura, J.-I., Awaji, S., and Kato, Y., 2008. Petrology and geochemistry of cross-chains in the Izu-Bonin back arc: three mantle components with contributions of hydrous liquids from a deeply subducted slab. *Geochemistry, Geophysics, Geosystems*, 9(5):Q05002. **http://dx.doi.org/10.1029/2007GC001641**

Manville, V., and Wilson, C.J.N., 2004. Vertical density currents: a review of their potential role in the deposition and interpretation of deep-sea ash layers. *Journal of the Geological Society,* 161(6):947–958. **http://dx.doi.org/10.1144/0016-764903-067**

McPhie, J., Doyle, M., and Allen, R., 1993. *Volcanic Textures: A Guide to the Interpretation of Textures in Volcanic Rocks:* Hobart (Tasmanian Government Printing Office).

Mitchell, S.F., 2000. Facies analysis of a Cretaceous–Paleocene volcaniclastic braid-delta. [presented at the Geological Society of Trinidad and Tobago 2000 SPE Conference and Exhibition, Port of Spain, Trinidad, 10–13 July 2000]. (Paper SS03)**http://archives.datapages.com/data/gstt/SS03F.PDF**

Orton, G.J., 1996. Volcanic environments. *In* Reading, H.G. (Ed.), *Sedimentary*

Environments: Processes, Facies and Stratigraphy: Oxford, UK (Blackwell Science Publishing), 485–573.

Palmer, B.A., and Walton, A.W., 1990. Accumulation of volcaniclastic aprons in the Mount Dutton Formation (Oligocene–Miocene), Marysvale volcanic field, Utah. *Geological Society of America Bulletin,* 102(6):734–748. **http://dx.doi.org/10.1130/0016-7606(1990)102<0734:AOVAIT>2.3.CO;2**

Pearce, J.A., Reagan, M.K., Stern, R.J., and Petronotis, K., 2013. Izu-Bonin-Mariana fore-arc: testing subduction initiation and ophiolite models by drilling the outer Izu-Bonin-Mariana fore arcfore-arc. *International Ocean Drilling Program Scientific Prospectus,* 352. **http://dx.doi.org/10.14379/iodp.sp.352.2013**

Plank, T., 2014. The chemical composition of subducting sediments. *In* Rudnick, R.L. (Ed.), *Treatise on Geochemistry* (2nd ed.) (Vol. 4): *The Crust*. Holland, H.D., and Turekian, K.K. (Series Eds.): Oxford (Elsevier), 607–629. **http://dx.doi.org/10.1016/B978-0-08-095975-7.00319-3**

Plank, T., and Langmuir, C.H., 1998. The chemical composition of subducting sediment and its consequences for the crust and mantle. *Chemical Geology,* 145(3–4):325–394.**http://dx.doi.org/10.1016/S0009-2541(97)00150-2**

Reading, H.G., and Richards, M., 1994. Turbidite systems in deep-water basin margins classified by grain size and feeder system. *AAPG Bulletin,* 78(5):792–822. **http://aapgbull.geoscienceworld.org/cgi/content/abstract/78/5/792**

Reagan, M.K., Ishizuka, O., Stern, R.J., Kelley, K.A., Ohara, Y., Blichert-Toft, J., Bloomer, S.H., Cash, J., Fryer, P., Hanan, B.B., Hickey-Vargas, R., Ishii, T., Kimura, J.-I., Peate, D.W., Rowe, M.C., and Woods, M., 2010. Fore-arc basalts and subduction initiation in the Izu-Bonin-Mariana system. *Geochemistry, Geophysics, Geosystems,* 11(3):Q03X12. **http://dx.doi.org/10.1029/2009GC002871**

Reagan, M.K., Pearce, J.A., Petronotis, K., and Expedition Scientists, 2015, Izu-Bonin-Mariana Fore Arc. Proceedings of the International Ocean Discovery Program, 352. International Ocean Discovery Program. http://dx.doi.org/10.14379/iodp.proc.352.2015.

Richards, M.T., 2009. Deep-marine clastic systems. *In* Emery, D., and Myers, K. (Eds.), *Sequence Stratigraphy:* London (Blackwell Science Publishing), 178–210. **http://dx.doi.org/10.1002/9781444313710.ch9**

Sample, J.C., and Karig, D.E., 1982. A volcanic production rate for the Mariana island arc. *Journal of Volcanology and Geothermal Research,* 13(1–2):73–82. **http://dx.doi.org/10.1016/0377-0273(82)90020-8**

Smith, G.A., 1987. Sedimentology of volcanism-induced aggradation in fluvial basins: examples from the Pacific Northwest, U.S.A. *In* Ethridge, F.G., Flores, R.M., and Harvey,

M.D. (Eds.), *Recent Developments in Fluvial Sedimentology*. Special Publication—SEPM (Society for Sedimentary Geology), 39:217–228. **http://dx.doi.org/10.2110/pec.87.39.0217**

Smith, G.A., and Landis, C., 1995. Intra-arc basins. *In* Busby, C.J., and Ingersoll, R.V. (Eds.), *Tectonics of Sedimentary Basins:* Oxford (Blackwell Science Publishing), 263–298.

Stern, R.J., Fouch, M.J., and Klemperer, S., 2003. An overview of the Izu-Bonin-Mariana subduction factory. *In* Eiler, J. (Ed.), *Inside the Subduction Factory*. Geophysical Monograph, 138:175–222. **http://dx.doi.org/10.1029/138GM10**

Stow, D.A.V., Reading, H.G., and Collinson, J.D., 1996. Deep seas. *In* Reading, H.G. (Ed.), *Sedimentary Environments: Processes, Facies and Stratigraphy:* Oxford, UK (Blackwell Science Publishing), 395–453.

Straub, S.M., 2003. The evolution of the Izu Bonin-Mariana volcanic arcs (NW Pacific) in terms of major elements. *Geochemistry, Geophysics, Geosystems,* 4(2):1018. **http://dx.doi.org/10.1029/2002GC000357**

Straub, S.M., Goldstein, S.L., Class, C., Schmidt, A., and Gomez-Tuena, A., 2010. Slab and mantle controls on the Sr–Nd–Pb–Hf isotope evolution of the post 42 Ma Izu–Bonin volcanic arc. *Journal of Petrology,* 51(5):993–1026. **http://dx.doi.org/10.1093/petrology/egq009**

Suyehiro, K., Takahashi, N., Ariie, Y., Yokoi, Y., Hino, R., Shinohara, M., Kanazawa, T., Hirata, N., Tokuyama, H., and Taira, A., 1996. Continental crust, crustal underplating, and low-*Q* upper mantle beneath an oceanic island arc. *Science,* 272(5260):390–392.**http://dx.doi.org/10.1126/science.272.5260.390**

Tamura, Y., and Tatsumi, Y., 2002. Remelting of an andesitic crust as a possible origin for rhyolitic magma in oceanic arcs: an example from the Izu-Bonin arc. *Journal of Petrology,* 43(6):1029–1047. **http://dx.doi.org/10.1093/petrology/43.6.1029**

Tamura, Y., Tatsumi, Y., Zhao, D., Kido, Y., and Shukuno, H., 2002. Hot fingers in the mantle wedge: new insights into magma genesis in subduction zones. *Earth and Planetary Science Letters,* 197(1–2):105–116. **http://dx.doi.org/10.1016/S0012-821X(02)00465-X**

Tamura, Y., Gill, J.B., Tollstrup, D., Kawabata, H., Shukuno, H., Chang, Q., Miyazaki, T., Takahashi, T., Hirahara, Y., Kodaira, S., Ishizuka, O., Suzuki, T., Kido, Y., Fiske, R.S., and Tatsumi, Y., 2009. Silicic magmas in the Izu-Bonin oceanic arc and implications for crustal evolution. *Journal of Petrology,* 50(4):685–723. **http://dx.doi.org/10.1093/petrology/egp017**

Tamura, Y., Ishizuka, O., Aoike, K., Kawate, S., Kawabata, H., Chang, Q., Saito, S.,

Tatsumi, Y., Arima, M., Takahashi, M., Kanamaru, T., Kodaira, S., and Fiske, R.S., 2010. Missing Oligocene crust of the Izu-Bonin arc: consumed or rejuvenated during collision? *Journal of Petrology,* 51(4):823–846. **http://dx.doi.org/10.1093/petrology/egq002**

Tamura, Y., Busby, C., and Blum, P., 2013. Izu-Bonin-Mariana Rear Arc: the missing half of the subduction factory. *International Ocean Discovery Program Scientific Prospectus,* 350. http://dx.doi.org/10.2204/iodp.sp.350.2013

Tamura, Y., Busby, C.J., Blum, P., Guèrin, G., Andrews, G.D.M., Barker, A.K., Berger, J.L.R., Bongiolo, E.M., Bordiga, M., DeBari, S.M., Gill, J.B., Hamelin, C., Jia, J., John, E.H., Jonas, A.-S., Jutzeler, M., Kars, M.A.C., Kita, Z.A., Konrad, K., Mahoney, S.H., Martini, M., Miyazaki, T., Musgrave, R.J., Nascimento, D.B., Nichols, A.R.L., Ribeiro, J.M., Sato, T., Schindlbeck, J.C., Schmitt, A.K., Straub, S.M., Vautravers, M.J., and Yang, Y., 2015a. Expedition 350 summary. *In* Tamura, Y., Busby, C.J., Blum, P., and the Expedition 350 Scientists, *Proceedings of the International Ocean Discovery Program, Expedition 350: Izu-Bonin-Mariana Rear Arc:* College Station, TX (International Ocean Discovery Program). http://dx.doi.org/10.14379/iodp.proc.350.101.2015

Tamura, Y., Busby, C.J., Blum, P., Guèrin, G., Andrews, G.D.M., Barker, A.K., Berger, J.L.R., Bongiolo, E.M., Bordiga, M., DeBari, S.M., Gill, J.B., Hamelin, C., Jia, J., John, E.H., Jonas, A.-S., Jutzeler, M., Kars, M.A.C., Kita, Z.A., Konrad, K., Mahoney, S.H., Martini, M., Miyazaki, T., Musgrave, R.J., Nascimento, D.B., Nichols, A.R.L., Ribeiro, J.M., Sato, T., Schindlbeck, J.C., Schmitt, A.K., Straub, S.M., Vautravers, M.J., and Yang, Y., 2015b. Expedition 350 methods. *In* Tamura, Y., Busby, C.J., Blum, P., and the Expedition 350 Scientists, *Proceedings of the International Ocean Discovery Program, Expedition 350: Izu-Bonin-Mariana Rear Arc:* College Station, TX (International Ocean Discovery Program). http://dx.doi.org/10.14379/iodp.proc.350.102.2015

Tamura, Y., Busby, C.J., Blum, P., Guèrin, G., Andrews, G.D.M., Barker, A.K., Berger, J.L.R., Bongiolo, E.M., Bordiga, M., DeBari, S.M., Gill, J.B., Hamelin, C., Jia, J., John, E.H., Jonas, A.-S., Jutzeler, M., Kars, M.A.C., Kita, Z.A., Konrad, K., Mahoney, S.H., Martini, M., Miyazaki, T., Musgrave, R.J., Nascimento, D.B., Nichols, A.R.L., Ribeiro, J.M., Sato, T., Schindlbeck, J.C., Schmitt, A.K., Straub, S.M., Vautravers, M.J., and Yang, Y., 2015c. Site U1436. *In* Tamura, Y., Busby, C.J., Blum, P., and the Expedition 350 Scientists, *Proceedings of the International Ocean Discovery Program, Expedition 350: Izu-Bonin-Mariana Rear Arc:* College Station, TX (International Ocean Discovery Program). http://dx.doi.org/10.14379/iodp.proc.350.103.2015

Tamura, Y., Busby, C.J., Blum, P., Guèrin, G., Andrews, G.D.M., Barker, A.K., Berger, J.L.R., Bongiolo, E.M., Bordiga, M., DeBari, S.M., Gill, J.B., Hamelin, C., Jia, J., John, E.H., Jonas, A.-S., Jutzeler, M., Kars, M.A.C., Kita, Z.A., Konrad, K., Mahoney, S.H., Martini, M., Miyazaki, T., Musgrave, R.J., Nascimento, D.B., Nichols, A.R.L., Ribeiro, J.M., Sato, T., Schindlbeck, J.C., Schmitt, A.K., Straub, S.M., Vautravers, M.J., and Yang, Y., 2015d. Site U1437. *In* Tamura, Y., Busby, C.J., Blum, P., and the Expedition 350 Scientists, *Proceedings of the International Ocean Discovery Program, Expedition 350:*

Izu-Bonin-Mariana Rear Arc: College Station, TX (International Ocean Discovery Program). http://dx.doi.org/10.14379/iodp.proc.350.104.2015

Taylor, B., 1992. Rifting and the volcanic-tectonic evolution of the Izu-Bonin-Mariana arc. *In* Taylor, B., Fujioka, K., et al., *Proceedings of the Ocean Drilling Program, Scientific Results,* 126: College Station, TX (Ocean Drilling Program), 627–651. **http://dx.doi.org/10.2973/odp.proc.sr.126.163.1992**

Taylor, B., Fujioka, K., et al., 1990. *Proceedings of the Ocean Drilling Program, Initial Reports,* 126: College Station, TX (Ocean Drilling Program).

Tollstrup, D., Gill, J., Kent, A., Prinkey, D., Williams, R., Tamura, Y., and Ishizuka, O., 2010. Across-arc geochemical trends in the Izu-Bonin arc: contributions from the subducting slab, revisited. *Geochemistry, Geophysics, Geosystems,* 11(1):Q01X10. **http://dx.doi.org/10.1029/2009GC002847**

Wright, I.C., 1996. Volcaniclastic processes on modern submarine arc stratovolcanoes: sidescan and photographic evidence from Rumble IV and V volcanoes, southern Kermadec arc (SW Pacific). *Marine Geology,* 136(1–2):21–39. **http://dx.doi.org/10.1016/S0025-3227(96)00054-0**

Yamashita Mikiya, Takahashi Narumi, Tamura Yoshihiko, Miura Seiichi, Kodaira Shuichi, 2017, Seismic imaging for an ocean drilling site survey and its verification in the Izu rear arc. *Exploration Geophysics* , -http://dx.doi.org/10.1071/EG16142

Yamazaki, T., and Stern, R.J., 1997. Topography and magnetic vector anomalies in the Mariana Trough. *JAMSTEC Deep Sea Research,* 13:31–45.

Yamazaki, T., and Yuasa, M., 1998. Possible Miocene rifting of the Izu–Ogasawara (Bonin) arc deduced from magnetic anomalies. *Island Arc,* 7(3):374–382. **http://dx.doi.org/10.1111/j.1440-1738.1998.00196.x**

CAPTIONS

Figure 1 – Tectonic setting of IBM arc (from Taylor, 1992; Tamura and Tatsumi, 2002). The IBM arc-trench system forms the convergent margin between the Pacific and Philippine Sea plates. Shown here are bathymetric features of the eastern Philippine Sea, IBM arc system, and Expedition 350 (Site U1436 in fore-arc and Site U1437 in rear arc)

and Expedition 351 and 352 site locations (EXP). Dashed lines = wide-angle seismic profiles; the north–south seismic profiles (along the present-day arc front and rear arc ~150 km west of the arc front) are shown in Figure 4. Lines of circles = conspicuous north–south rows of long-wavelength magnetic anomalies, attributed to loci of Oligocene magmatic centers by Yamazaki and Yuasa (1998). Site U1436 is on the fore-arc anomaly (fore-arc high/Shin-Kurose Ridge); Site U1437 is on the rear-arc anomaly (Nishi-shichito Ridge). The boundary between the Izu arc and the Bonin arc lies at the Sofugan Tectonic Line, discussed further in Figure 4.

Figure 2 - Wide-angle seismic profile across the Izu arc, with *P*-wave velocities for upper, middle, and lower crust (greens) and for mantle (blues) (Suyehiro et al., 1996). ODP (black) and IODP (red) sites are projected onto this line of section. Site U1437 is the first site drilled in the broad region of long-lived rear-arc seamount chains (shown on Figure 3). ODP Site 791 is also in the rear arc, but it is located in the narrow, young, and active Sumisu rift. Site U1436 and ODP Sites 792, 793, and 786 are in the modern fore-arc basin. BON = boninite, FAB = fore-arc basalt.

Figure 3 - Volcano-tectonic domains within Izu arc. The well-defined arc front is formed by a ~north-south chain of island volcanoes, the largest of which are named here. Arc crust underlies the rear arc, whereas the Shikoku Basin (Figure 1), which forms the western boundary of the rear arc, is floored by oceanic crust. The rear arc is divided into two tectonic zones, from west to east (also oldest to youngest): (1) rear-arc seamount chains (~100 km long; ~17-3 Ma) which trend at a high angle to the arc front and span

1350 the compositional range from basalt to rhyolite, and (2) extensional zone (~100 km wide,
1351 <3 Ma), overlapping the eastern half of the rear-arc seamount chains, and characterized
1352 by ~north-south normal faults with small bimodal volcanoes (backarc knolls). Along the
1353 eastern margin of the extensional zone, immediately behind the arc front, lies a narrow
1354 active rift (<1 Ma), with north-south rift basins and bimodal volcanism. Volcanic rocks in
1355 the extensional zone and the active rift are referred to as rift-type magmas, and those in
1356 the rear-arc seamount chains are referred to as rear-arc seamount chain-type magmas.
1357 White stars = Site U1436 (fore-arc) and Site U1437 (rear arc). Box = area of Figure 7.
1358
1359 Figure 4 - Wide-angle seismic profiles (Kodaira et al., 2008) showing middle-crust
1360 thickness variations in two transects: one along the arc front and one along the rear-arc
1361 Nishi-shichito Ridge; the positions of these lines are shown as lines of circles on Figure
1362 1. The 6.0–6.8, 7.1–7.3, and 7.8 km/s layers (see P wave velocity on key) correspond to
1363 middle crust, lower crust, and upper mantle, respectively. Based on variations in middle-
1364 crust thickness in these profiles, Kodaira et al. (2008) infer that rear-arc crust was
1365 obliquely rifted off the arc front, probably during the opening of the Shikoku and Parece
1366 Vela Basins (~25 Ma; Figure 1). Quaternary basalt-dominant island volcanoes on the arc
1367 front: Mi = Miyakejima, Ha = Hachijojima, Ao = Aogashima, Su = Sumisu Caldera, To =
1368 Torishima; andesite Oligocene volcano east of arc front: Om = Omachi Seamount. ODP
1369 Sites 787, 792, and 793 also shown.
1370
1371 Figure 5 - Hot fingers hypothesis of Tamura et al. (2002) proposed for northeast Japan
1372 and adapted here for the origin of Izu rear-arc seamount chains. Hypothetically, mantle

convection above the subducting slab produces fingerlike hot regions in the mantle wedge below the rear-arc plate. These hot regions extend toward the arc front with time, suggesting younging of rear-arc seamounts from west to east.

Figure 6 - Two main basin types recognized within arcs, as defined by Smith and Landis (1995). A. Volcano-bounded basin: small, irregular basins between individual volcanoes; larger linear troughs between volcanic chains; and thick basin fill preserved only in oceanic arcs, below sea level. Low areas between the series of rear-arc seamount chains shown on Figure 3 are volcano-bounded basins formed during growth of the chains between ~17 and 3 Ma. Site U1437 is located in one of these volcano-bounded basins, which we refer to as the Enpo-Manji Basin (Figures7, 8C, 8D). B. Fault-bounded basin: rapidly subsiding basins that are deep (up to 10 km) and have very high sediment accumulation rates (~1 km/My); they are found in continental and oceanic arcs. A fault-bounded basin is currently forming in the <1 Ma active rift west of the Izu arc front (Figure 3). Although the broader zone of extension (<3 Ma) produced faults within the eastern halves of the volcano-bounded basins between the rear-arc seamount chains, including the basin drilled at Site U1437 (some visible on Figures 8C, 8D), the bounding volcanic chains (and not the <3 Ma extensional zone faults) primarily controlled accommodation (Figure 8C).

Figure 7 - Bathymetric maps of rear-arc region behind the arc-front volcanoes (location on Figure 3). (A) Unannotated and annotated bathymetric maps, showing named volcanoes and $^{40}Ar/^{39}Ar$ and K-Ar ages in Ma from Ishizuka et al. (2003b). Age groups:

~12.5–3 Ma rear-arc basalt to rhyolite seamount volcanoes, <3 Ma bimodal volcanic rocks in extension zone that overlaps eastern half of the rear-arc seamount chains, and <1 Ma bimodal volcanic rocks of the narrow active rift (Figure 3). Site U1437 lies in a volcano-bounded basin (Figure 6A) between the Manji and Enpo rear-arc seamount chains at the foot of flat-topped Manji Volcano, presumably planed by wave action. (B) Positions of JAMSTEC surveys (Yamashita et al., 2015) shown in Figure 8.

Figures 8 – Three seismic lines, crossing at Site U1437 (Yamashita et al., 2008); positions plotted on Figure 7B. Line IBr5 is the longest, an ~E-W line that runs from the Manji rear-arc seamount chain in the west to the arc front in the east. This is shown as: (A) Line IBr5 OBS: seismic velocity image obtained from wide-angle OBS data, with OBSs deployed every 5 km along Line IBr5, and (B) Line IBr5 MCS, depth-converted MCS reflection profile; dashed yellow lines = iso-velocity contours of 5 and 6 km/s obtained from seismic velocity image in (A), which are interpreted as the depth to igneous basement (upper crust) and middle crust, respectively. Seismic lines with interpreted seismic layers are shown in (C) and (D), running transverse to the Enpo-Manji volcano-bounded basin (C) and along the axis of the basin (D). On (C), the Manji volcano lies on the northwest, with $^{40}Ar/^{39}Ar$ ages of 6.86 and 6.53 Ma, and an unnamed volcano lies on the southeast, with an $^{40}Ar/^{39}Ar$ age of 1.96 Ma (see Figure 7). On (D), an unnamed volcano lies on the southwest, with an 40Ar/39Ar age of 12.35 Ma; minor north-northwest faults lie transverse to the volcano-bounded basin, parallel to normal faults in the broad extensional zone to the east (Figure 3). The north-northwest faults

1418 appear to have been active prior to the deposition of Layer L3 but do not provide the
1419 primary accommodation.
1420
1421 Figure 9 – Age-depth model for Site U1437. Shown are shipboard biostratigraphic and
1422 magnetostratigraphic datums, and LSR (linear sedimentation rates)/MAR (mass
1423 accumulation rates). MARs are calculated using LSR derived from the age-depth model
1424 and dry bulk density calculated from shipboard moisture and density (MAD) analyses.
1425 MARs of carbonate (CAR) and noncarbonated (nCAR) are calculated by multiplying the
1426 MAR by carbonate weight percent, calculated from shipboard coulometry measurements
1427 of inorganic carbon weight percent. T = top, B = bottom, X = crossover.
1428
1429 Figure 10 - Summary lithostratigraphic log for Site U1437. The boundary between
1430 coarse- and fine-grained volcaniclastics is 2 mm (corresponding to the boundary between
1431 ash and lapilli-sized particles). Representative core photos for Lithostratigraphic Units I
1432 through VI and Igneous Unit 1 are shown in Figures 11 to 18.
1433
1434 Figure 11 – Unit I, representative core photos and interpretations: (Left pair) 5–10 cm
1435 mafic ash intervals with sharp bases and tops grading upward into tuffaceous mud, with
1436 mafic ash pods. (Right pair) Evolved tuff intervals grading upward into tuffaceous mud
1437 and bioturbation.
1438
1439 Figure 12 – Unit II, core photos and line drawings of closely intercalated monomictic
1440 tuff, lapilli-tuff, and lapillistone, showing stratification, cross stratification, and normal

1441 grading. Crystal-rich tuff (1), lapilli-tuff (2), and lapillistone (3) in planar and cross-
1442 bedded intervals.
1443
1444 Figure 13 - Unit III, core photos: (a) Alternating intervals of tuffaceous mudstone,
1445 evolved tuff, and evolved lapilli-tuff. (b) Intercalated white to gray-green evolved tuff,
1446 including soft-sediment deformation. (c) Crystal-rich stratified interval. (d) Fiamme-rich
1447 (with flattened pumice) and (nonflattened) pumice-rich intercalated layers.
1448
1449 Figure 14 - Unit IV: (a) Line scan and schematic drawing showing tuff, clast-supported
1450 polymictic lapilli-tuff, and fine-grained light green tuff lithofacies. (b) Line scan and
1451 schematic drawing of tuff and clast-supported polymictic lapilli-tuff lithofacies. (c) Fine-
1452 grained light green tuff, including: 1. sand-sized tuff with planar stratification, and 2. silt-
1453 sized vitric light green tuff with convolute bedding. (d) Photomicrographs of lapillistone
1454 and lapilli-tuff (plane-polarized light): 1. Lapillistone dominated by plagioclase-phyric
1455 andesite clasts with minor pumice clasts. 2. Lapilli-tuff with pumice clasts and fiamme.
1456
1457 Figure 15 - Unit V: (a) Monomictic reversely graded lapilli-tuff with tuffaceous
1458 mudstone. The lapilli are made of flattened pumice (fiamme) or nonflattened pumice.
1459 Note the erosive base and reverse coarse-tail grading of lapilli, with upward-increasing
1460 tuffaceous mudstone. (b) Annotated line scan of soft-sediment faulting in tuff, Unit V. (c)
1461 Lapilli-tuff and lapillistone: 1. White to light gray lapilli-tuff with large pumice lapillus.
1462 The matrix is composed of glass shards, smaller pumice lapilli, and plagioclase; 2. Clast-
1463 supported dark gray-green lapilli-tuff showing pumice lapilli and volcanic lithic clasts,

plagioclase, and opaques; 3. Clast-supported dark gray-green lapilli-tuff with crystals of pyroxene, plagioclase, and opaques; the large feldspars have visible melt inclusions.

Figure 16 - Unit VI: (a) Clast-supported polymictic lapilli-tuff with subrounded pumice and lithic clasts of rounded mafic and evolved volcanics. (b) Clast-supported polymictic lapillistone with pumice and lithic clasts of subrounded tuffaceous mudstone and evolved volcanics. (c) Stratification in a tuff layer with subordinate fiamme, in macroscopic view, and (d) in microscopic view. (e) Microscopic view of clast-supported polymictic lapilli-tuff. (f) Microscopic view of matrix-supported polymictic lapilli-tuff. (g) Andesite clast with plagioclase, clinopyroxene, and opaques (plane-polarized light). Red box = location of photomicrographs shown in (h) plane-polarized light and (i) cross-polarized light.

Figure 17 - Igneous Unit 1 intrusive rhyolite: (a) Igneous Unit 1 and its intrusive relationship with Unit VI. Only 1.21 m was recovered but its true thickness may be up to 6.50 m (see text). A second interval of similar material lower in the core (labeled "?") is only 5 cm thick and has no recovered contacts; it was therefore described as a clast (note that similar clasts are described from the host Unit VI). Continued on next page: (b) Upper contact on igneous Unit 1 intrusive rhyolite and relationship with its Unit VI host; for discussion, see text. Photomicrographs of the (1, 2) margin and (3, 4) interior show the chilled upper margin of igneous Unit 1. (c) Peperitic lower contact on igneous Unit 1 intrusive rhyolite.

Figure 18 - Unit VII: (a) Representative photo of 84 m thick nongraded, nonstratified, black glassy lapillistone and lapilli tuff: consists of nonvesicular glass particles with plagioclase and pyroxene phenocrysts and glomerocrysts, with no bubble-wall shards or broken crystals. (b) Plane-polarized light and (c) cross-polarized light photomicrograph of andesite clast containing plagioclase (Plag) and clinopyroxene (Cpx) in a glass groundmass. (d) Plane-polarized light and (e) cross-polarized light photomicrograph of jigsaw-fit and randomly distributed andesite glassy clasts with poorly inflated breadcrust textures. (f) Matrix-supported lapilli-tuff showing clasts with quenched margins and breadcrust texture. (g) Chilled margin around amygdaloidal andesite lithic clast surrounded by lapilli-tuff.

Figure 19 - Petrophysical data from cores (whole-round core section logging, black dots; section half measurements, green crosses; discrete samples, blue crosses) and from downhole logging (red lines). Three holes were cored at Site U1437 (B, D, E) with core recovery shown in the left-most column (black = recovered, white = not recovered). GRA = Gamma Ray Attenuation method. PWC = P-Wave Caliper method. MAD = Moisture And Density method. Log RT = "True resistivity" from downhole logging. Mag. Susc. = magnetic susceptibility. Bulk density estimates from the MAD method used on cores match very well the values obtained with the GRA method in downhole logs. Density values using GRA on cores (black dots) are underestimated because (1) calibration is routinely performed for 66 mm diameter cores (as in Hole U1437B) and not the 58 mm diameter cores of Holes U1437D and E; and (2) core disturbance (gaps, cracks, washouts) result in even lower values. These data are useful for the detection of core

1509 disturbance and they can be partially corrected for a high-resolution density record with
1510 some effort. Porosity and P-wave velocity values obtained from cores and from logs
1511 match well despite the different methods, tools and scales employed. Magnetic
1512 susceptibility values are arbitrary instrument units from both core and downhole detectors
1513 and we bring the values to the same scale by multiplying the log values with 10^5 and
1514 adding 30. Natural gamma radiation values from cores are in instrument-specific counts/s
1515 unit, whereas those from downhole logs are calibrated according to the American
1516 Petroleum Institute (API) standard and expressed as gAPI. We chose to bring the core
1517 and log records to the same scale by multiplying the core data by 1.4 and adding 8.
1518 Technical difficulties prohibited downhole logging in Hole U1437E. Gray lines delineate
1519 lithologic unit boundaries (Roman numerals in Lith. Units column). Purple lines (appear
1520 as one line) represent the nominally 1.2-m thick igneous unit 1.
1521
1522 Figure 20 - Zr/Y vs. SiO2 for volcaniclastic and igneous samples from sedimentary Units
1523 I–VII and igneous Unit 1 (Site U1437) (below), compared to literature data from Izu arc
1524 and from the Izu arc (above). Literature data include: rear arc volcanoes, shown in blue;
1525 arc front basalt-dominated island volcanoes with small volumes of rhyolite (R1 type
1526 rhyolite), shown in red; and arc front rhyolite-dominant submarine calderas (R2 type
1527 rhyolite), shown in black. R1 and R2 rhyolites defined by Tamura et al. (2009). Literature
1528 data sources: Tamura et al. (2009), Gill et al. (1994), Bryant et al. (2003), Straub et al.
1529 (2003, 2010), Hochstaedter et al. (2001), Ishizuka et al. (2002, 2003a, 2003b, 2006a,
1530 2006b), Machida et al. (2003, 2008), Tollstrup et al. (2010). Samples from Units I
1531 through V (upper 1320 m) lie in both the arc front and rear arc fields, consistent with

their fine grain size, which may be distal from sources. In contrast, Units VI and VII (lower 25% of section) are coarse-grained, vent-proximal deposits (see text), and igneous Unit 1 is an intrusion and thus also vent-proximal; however, these plot mainly in the arc front field, despite their position in the rear arc. This suggests that rear arc magmas only fully compositionally diverged after ca. 13 Ma. (Note: One outlier contains anomalously high Zr/Y and is not included in the fields).

Figure 21 - Zr and Zr/Y analyzed by pXRF and ICP-AES for volcaniclastic and igneous samples, Site U1437. Probability curves below depth panels show the relative distribution of Zr and Zr/Y in basalt-dominant island volcanoes from the arc front (including R1 rhyolites), rhyolite-dominant submarine calderas in the arc front (R2 rhyolites), and rear-arc volcanic rocks. Vertical lines = composition of the peaks in the literature data distributions. Ig1 = igneous Unit 1. Data sources: Tamura et al. (2009), Gill et al. (1994), Bryant et al. (2003), Straub et al. (2003, 2010), Hochstaedter et al. (2001), Ishizuka et al. (2002, 2003a, 2003b, 2006a, 2006b), Machida et al. (2003, 2008), Tollstrup et al. (2010).

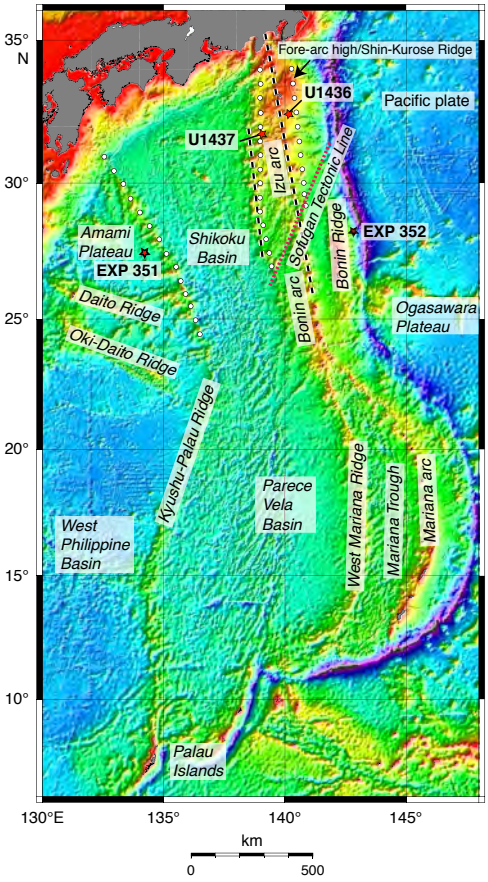
35°
N
30°
25°
20°
15°
10°
130°E
135°
140°
145°
km
0
500
Fore-arc high/Shin-Kurose Ridge
U1436
Pacific plate
U1437
Izu arc
Sofugan Tectonic Line
Bonin Ridge
EXP 352
Amami
Plateau
EXP 351
Shikoku
Basin
Bonin arc
Ogasawara
Plateau
Daito Ridge
Oki-Daito Ridge
Kyushu-Palau Ridge
Parece
Vela
Basin
West Mariana Ridge
Mariana Trough
Mariana arc
West
Philippine
Basin
Palau
Islands

Figure 1

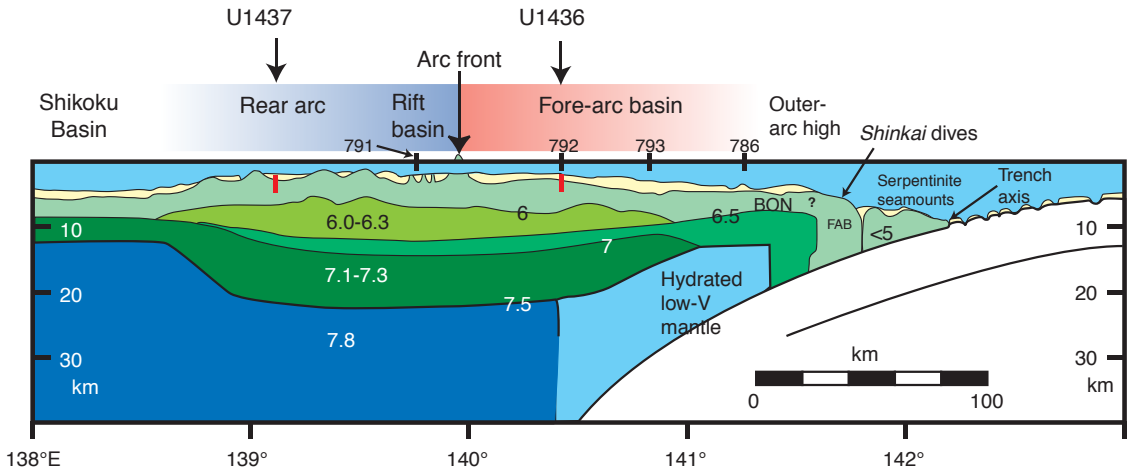
U1437
U1436
Arc front
Shikoku Basin
Rear arc
Rift basin
Fore-arc basin
Outer-arc high
Shinkai dives
791
792
793
786
Serpentinite seamounts
Trench axis
6.0-6.3
6
6.5
BON
?
FAB
<5
10
7
7.1-7.3
20
7.5
Hydrated low-V mantle
7.8
30
km
km
0
100
10
20
30
km
138°E
139°
140°
141°
142°

Figure 2

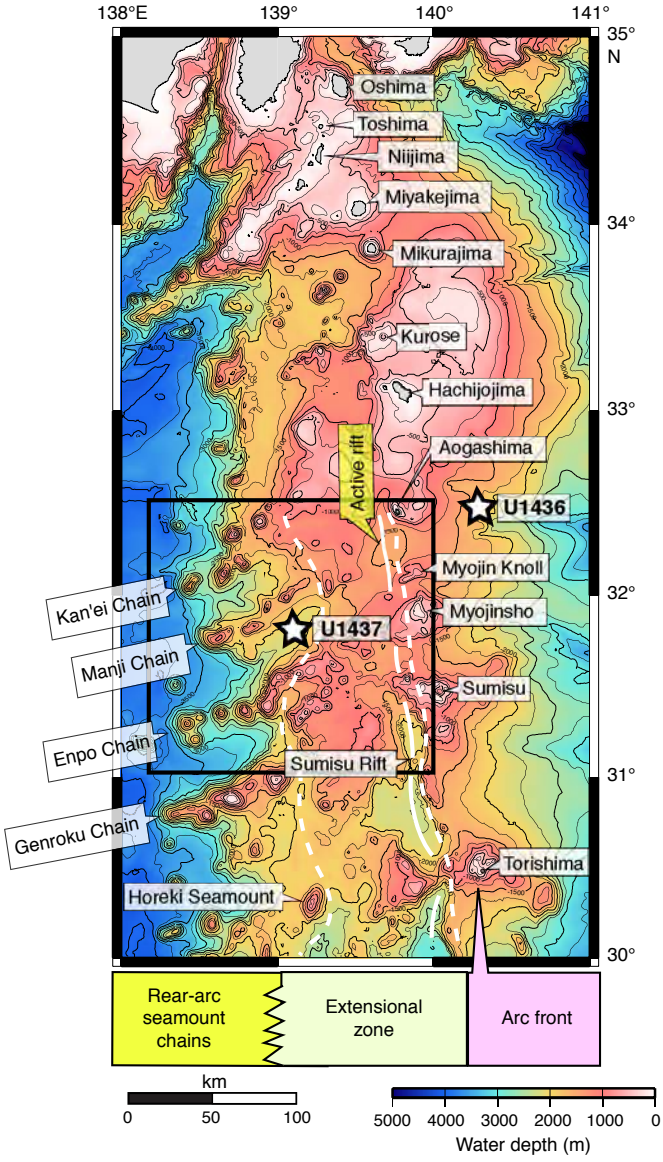
138°E
139°
140°
141°
35° N
34°
33°
32°
31°
30°
Oshima
Toshima
Niijima
Miyakejima
Mikurajima
Kurose
Hachijojima
Aogashima
Active rift
U1436
Myojin Knoll
Myojinsho
U1437
Sumisu
Sumisu Rift
Kan'ei Chain
Manji Chain
Enpo Chain
Genroku Chain
Horeki Seamount
Torishima
Rear-arc seamount chains
Extensional zone
Arc front
km
0
50
100
5000
4000
3000
2000
1000
0
Water depth (m)

Figure 3

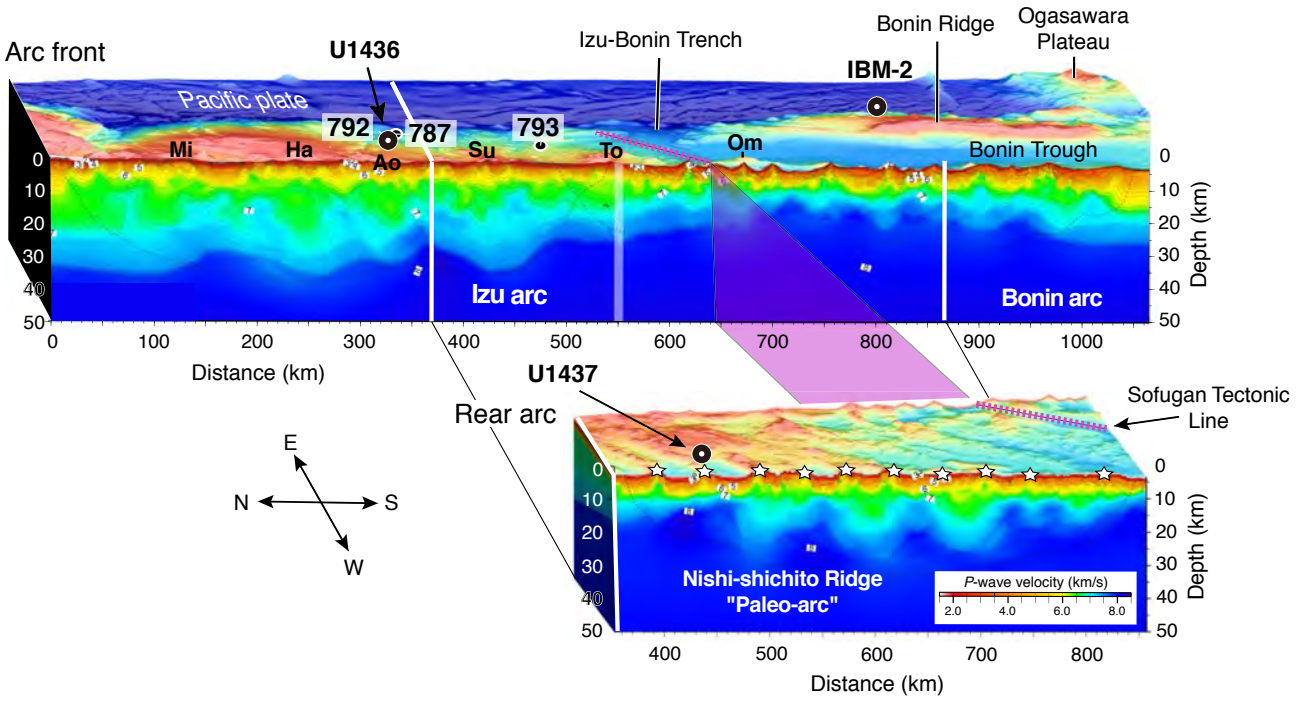
Arc front
U1436
Izu-Bonin Trench
Bonin Ridge
Ogasawara Plateau
IBM-2
Pacific plate
792
787
793
Mi
Ha
Ao
Su
To
Om
Bonin Trough
Izu arc
Bonin arc
Distance (km)
Depth (km)
U1437
Rear arc
Sofugan Tectonic Line
E
N
S
W
Nishi-shichito Ridge
"Paleo-arc"
P-wave velocity (km/s)
2.0
4.0
6.0
8.0

Figure 4

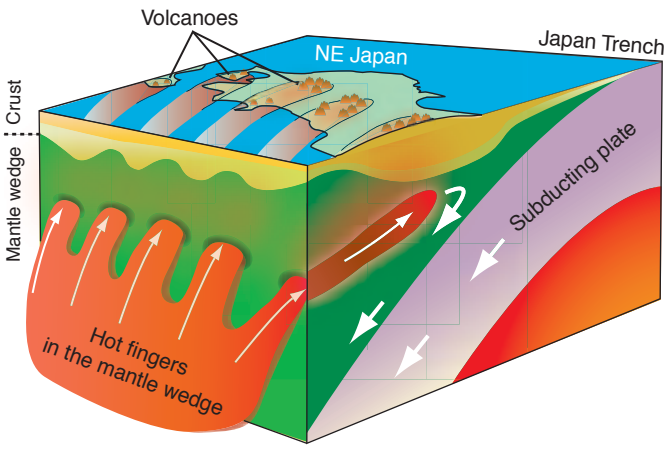
Volcanoes
NE Japan
Japan Trench
Crust
Mantle wedge
Subducting plate
Hot fingers
in the mantle wedge

Figure 5

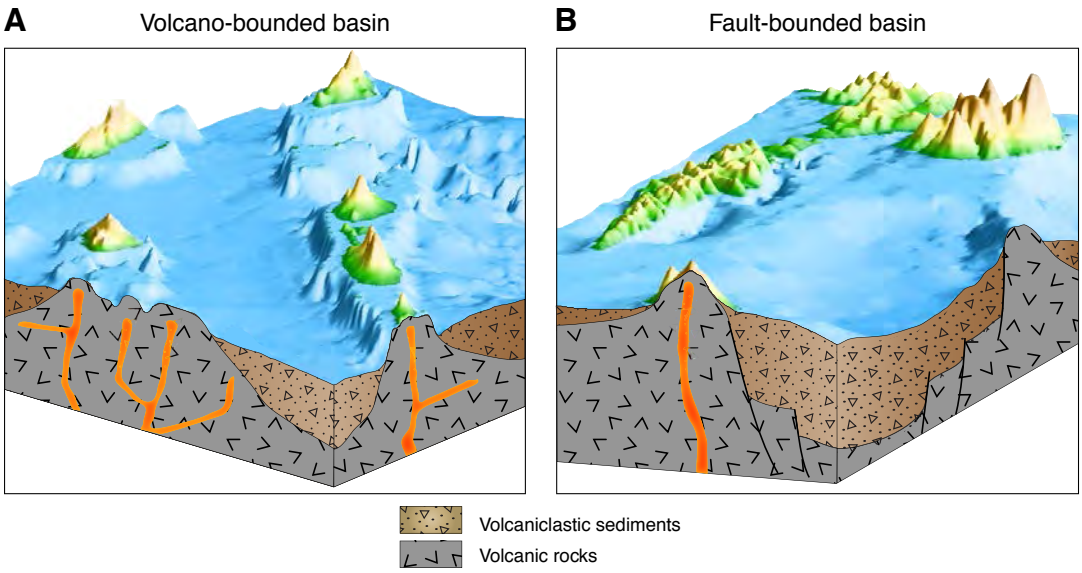
A
Volcano-bounded basin
B
Fault-bounded basin
Volcaniclastic sediments
Volcanic rocks

Figure 6

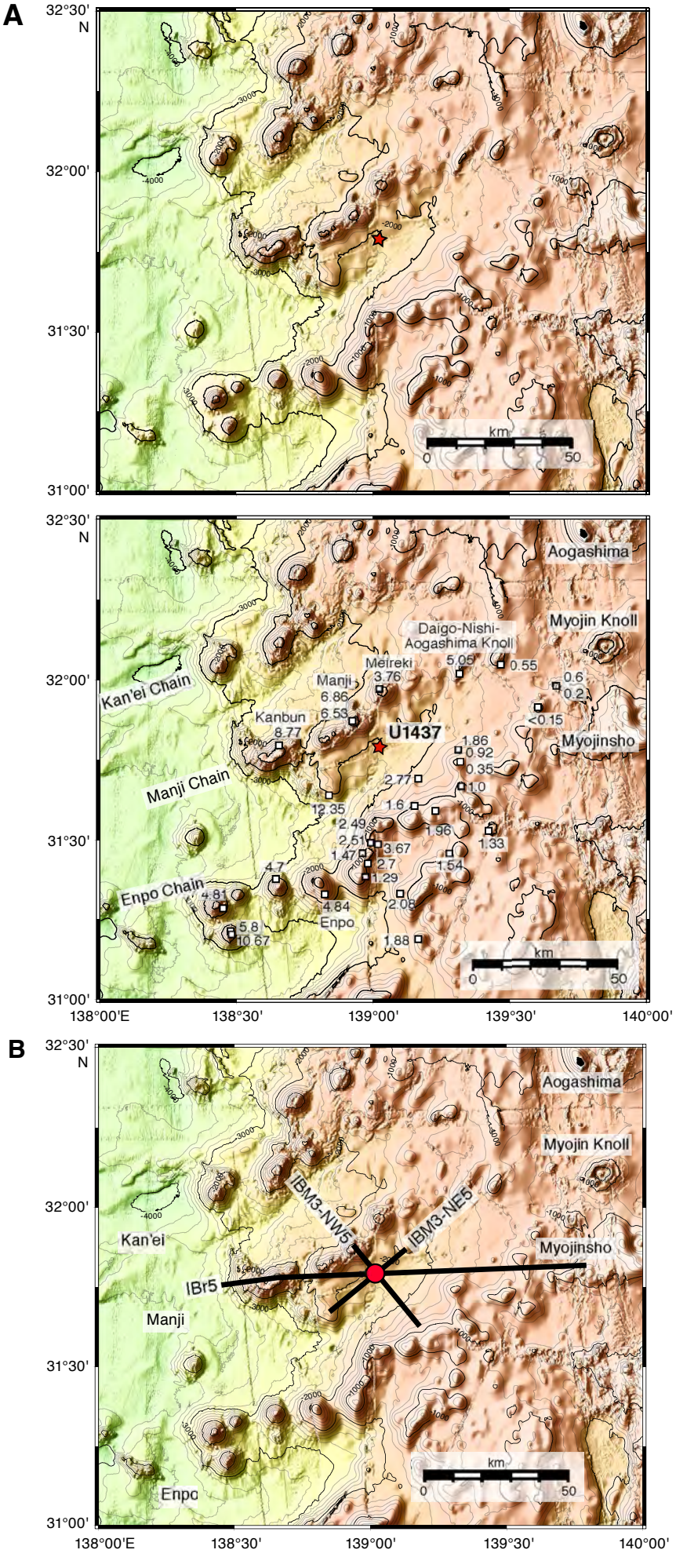
A
32°30' N
32°00'
31°30'
31°00'
km
0
50
Aogashima
Myojin Knoll
Daigo-Nishi-Aogashima Knoll
Meireki
Manji
Kanbun
Kan'ei Chain
Manji Chain
Enpo Chain
U1437
Myojinsho
Enpo
3.76
6.86
6.53
8.77
5.05
0.55
0.6
0.2
<0.15
1.86
0.92
0.35
2.77
1.0
1.6
1.96
1.33
12.35
2.49
2.51
3.67
1.47
2.7
1.29
1.54
4.7
4.81
4.84
2.08
5.8
10.67
1.88
138°00'E
138°30'
139°00'
139°30'
140°00'
B
IBM3-NW5
IBM3-NE5
IBr5
Kan'ei
Manji
Enpo

Figure 7

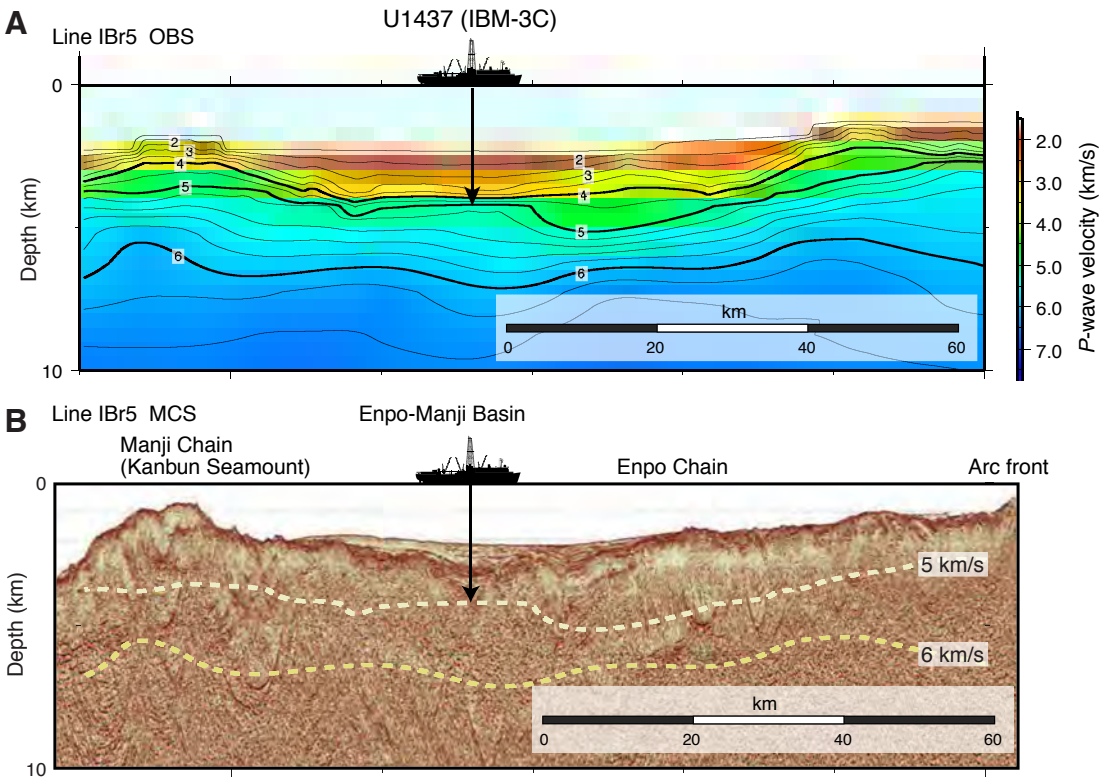
A
Line IBr5 OBS
U1437 (IBM-3C)
0
10
Depth (km)
2
3
4
5
6
km
0
20
40
60
2.0
3.0
4.0
5.0
6.0
7.0
P-wave velocity (km/s)
B
Line IBr5 MCS
Enpo-Manji Basin
Manji Chain
(Kanbun Seamount)
Enpo Chain
Arc front
0
10
Depth (km)
5 km/s
6 km/s
km
0
20
40
60

Figure 8A, 8B

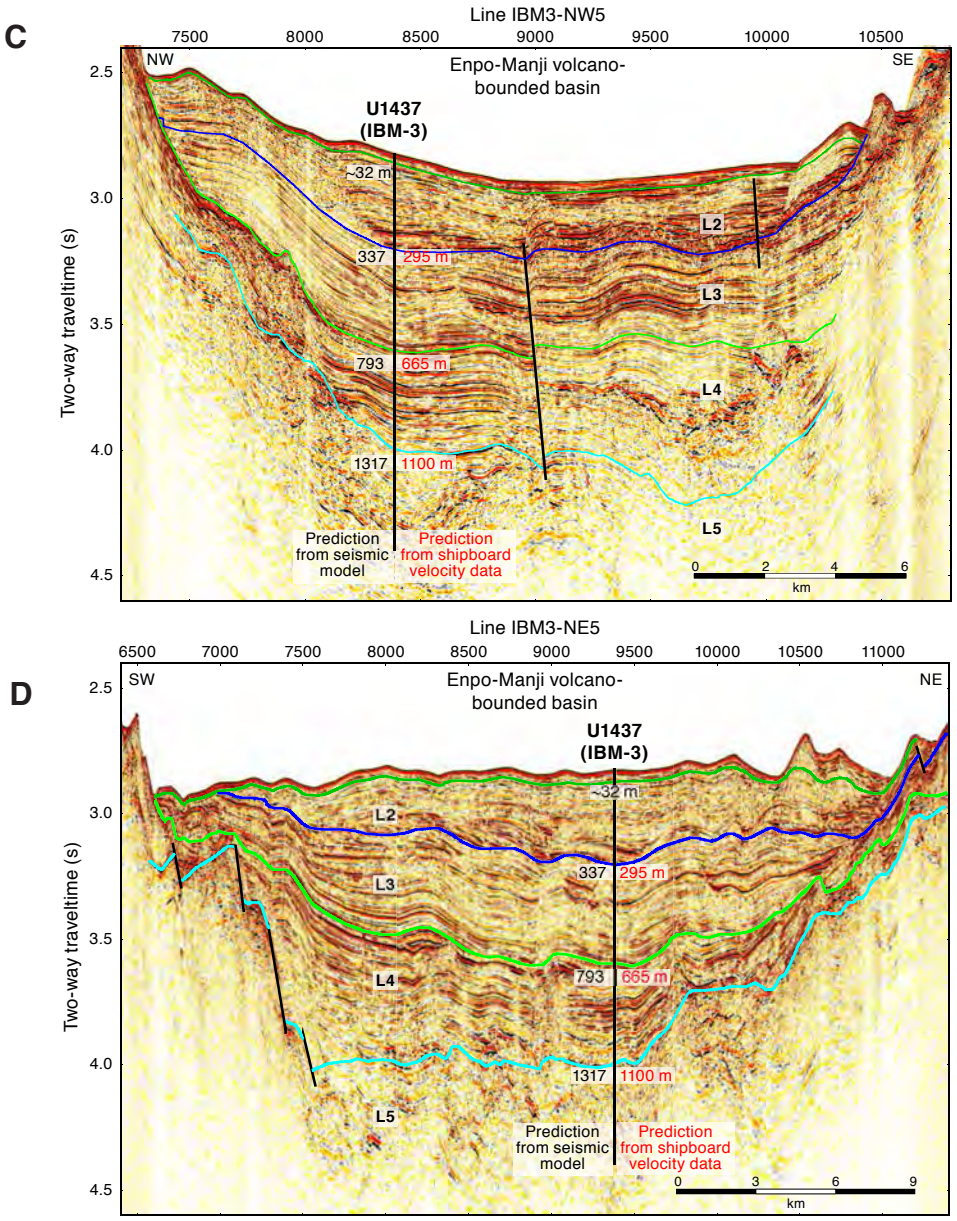
C
Line IBM3-NW5
7500
8000
8500
9000
9500
10000
10500
NW
SE
Enpo-Manji volcano-bounded basin
U1437 (IBM-3)
~32 m
337
295 m
793
665 m
1317
1100 m
L2
L3
L4
L5
Prediction from seismic model
Prediction from shipboard velocity data
0
2
4
6
km
Two-way traveltime (s)
2.5
3.0
3.5
4.0
4.5
D
Line IBM3-NE5
6500
7000
7500
8000
8500
9000
9500
10000
10500
11000
SW
NE
Enpo-Manji volcano-bounded basin
U1437 (IBM-3)
~32 m
337
295 m
793
665 m
1317
1100 m
L2
L3
L4
L5
Prediction from seismic model
Prediction from shipboard velocity data
0
3
6
9
km
Two-way traveltime (s)
2.5
3.0
3.5
4.0
4.5

Figure 8C, 8D

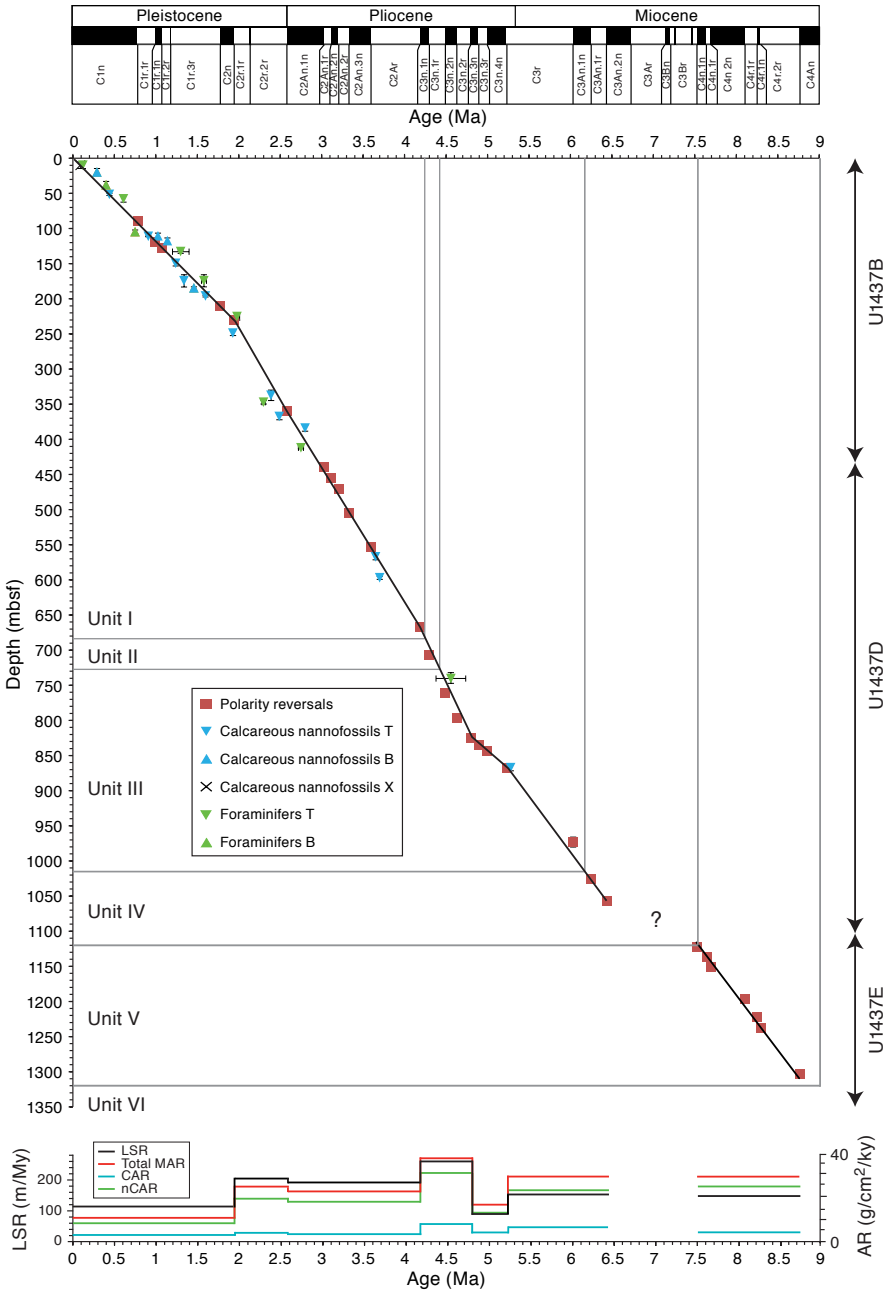
Pleistocene
Pliocene
Miocene
C1n
C1r.1r
C1r.1n
C1r.2r
C1r.3r
C2n
C2r.1r
C2r.2r
C2An.1n
C2An.1r
C2An.2n
C2An.2r
C2An.3n
C2Ar
C3n.1n
C3n.1r
C3n.2n
C3n.2r
C3n.3n
C3n.3r
C3n.4n
C3r
C3An.1n
C3An.1r
C3An.2n
C3Ar
C3Bn
C3Br
C4n.1n
C4n.1r
C4n.2n
C4r.1r
C4r.1n
C4r.2r
C4An
Age (Ma)
Depth (mbsf)
Unit I
Unit II
Unit III
Unit IV
Unit V
Unit VI
Polarity reversals
Calcareous nannofossils T
Calcareous nannofossils B
Calcareous nannofossils X
Foraminifers T
Foraminifers B
?
U1437B
U1437D
U1437E
LSR
Total MAR
CAR
nCAR
LSR (m/My)
AR (g/cm2/ky)
Age (Ma)

Figure 9

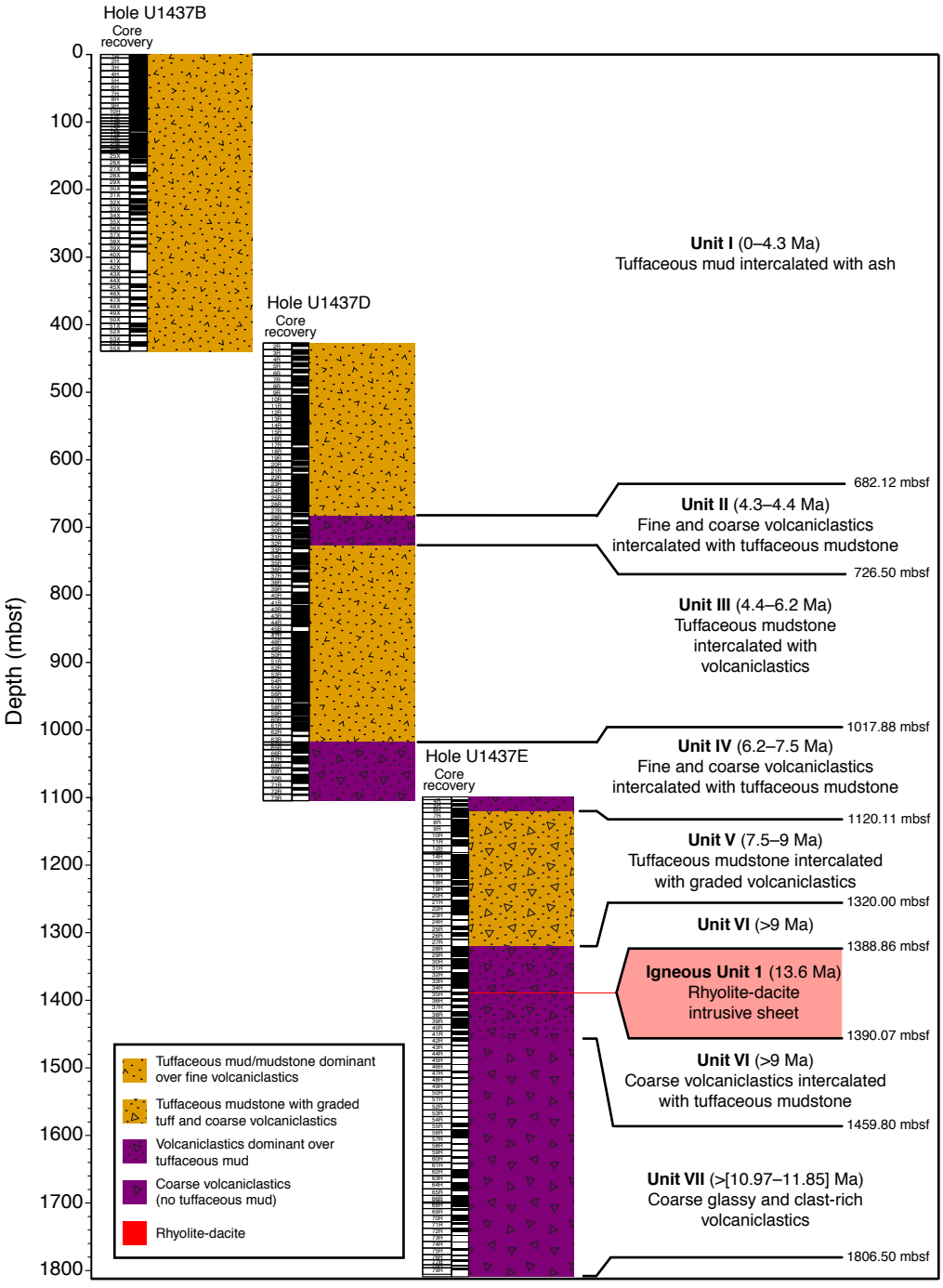
Hole U1437B
Core recovery
Hole U1437D
Core recovery
Hole U1437E
Core recovery
Depth (mbsf)
0
100
200
300
400
500
600
700
800
900
1000
1100
1200
1300
1400
1500
1600
1700
1800
Unit I (0–4.3 Ma)
Tuffaceous mud intercalated with ash
682.12 mbsf
Unit II (4.3–4.4 Ma)
Fine and coarse volcaniclastics intercalated with tuffaceous mudstone
726.50 mbsf
Unit III (4.4–6.2 Ma)
Tuffaceous mudstone intercalated with volcaniclastics
1017.88 mbsf
Unit IV (6.2–7.5 Ma)
Fine and coarse volcaniclastics intercalated with tuffaceous mudstone
1120.11 mbsf
Unit V (7.5–9 Ma)
Tuffaceous mudstone intercalated with graded volcaniclastics
1320.00 mbsf
Unit VI (>9 Ma)
1388.86 mbsf
Igneous Unit 1 (13.6 Ma)
Rhyolite-dacite intrusive sheet
1390.07 mbsf
Unit VI (>9 Ma)
Coarse volcaniclastics intercalated with tuffaceous mudstone
1459.80 mbsf
Unit VII (>[10.97–11.85] Ma)
Coarse glassy and clast-rich volcaniclastics
1806.50 mbsf
Tuffaceous mud/mudstone dominant over fine volcaniclastics
Tuffaceous mudstone with graded tuff and coarse volcaniclastics
Volcaniclastics dominant over tuffaceous mud
Coarse volcaniclastics (no tuffaceous mud)
Rhyolite-dacite

Figure 10

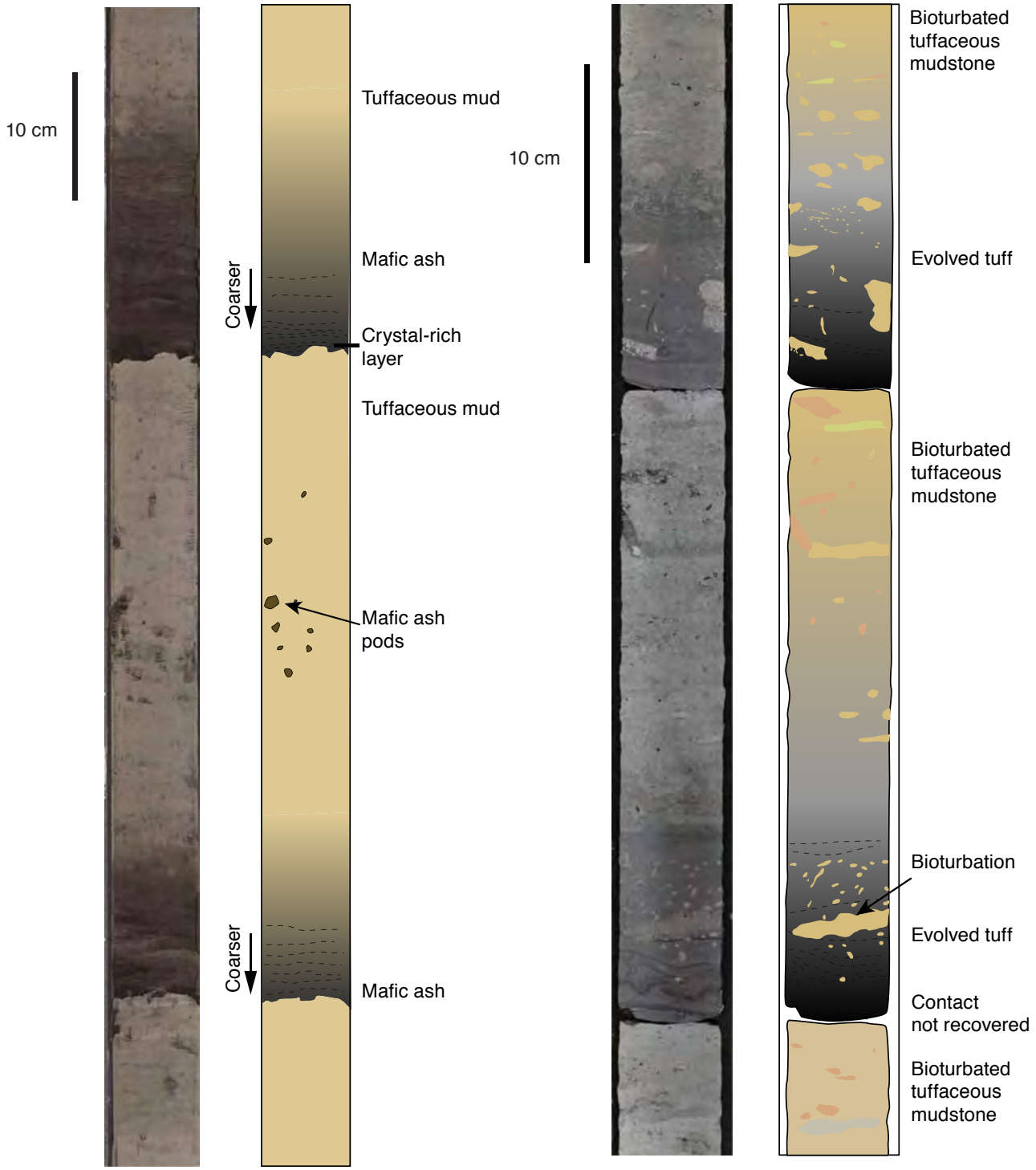
10 cm
Tuffaceous mud
Mafic ash
Coarser
Crystal-rich layer
Tuffaceous mud
Mafic ash pods
Coarser
Mafic ash
10 cm
Bioturbated tuffaceous mudstone
Evolved tuff
Bioturbated tuffaceous mudstone
Bioturbation
Evolved tuff
Contact not recovered
Bioturbated tuffaceous mudstone

Figure 11

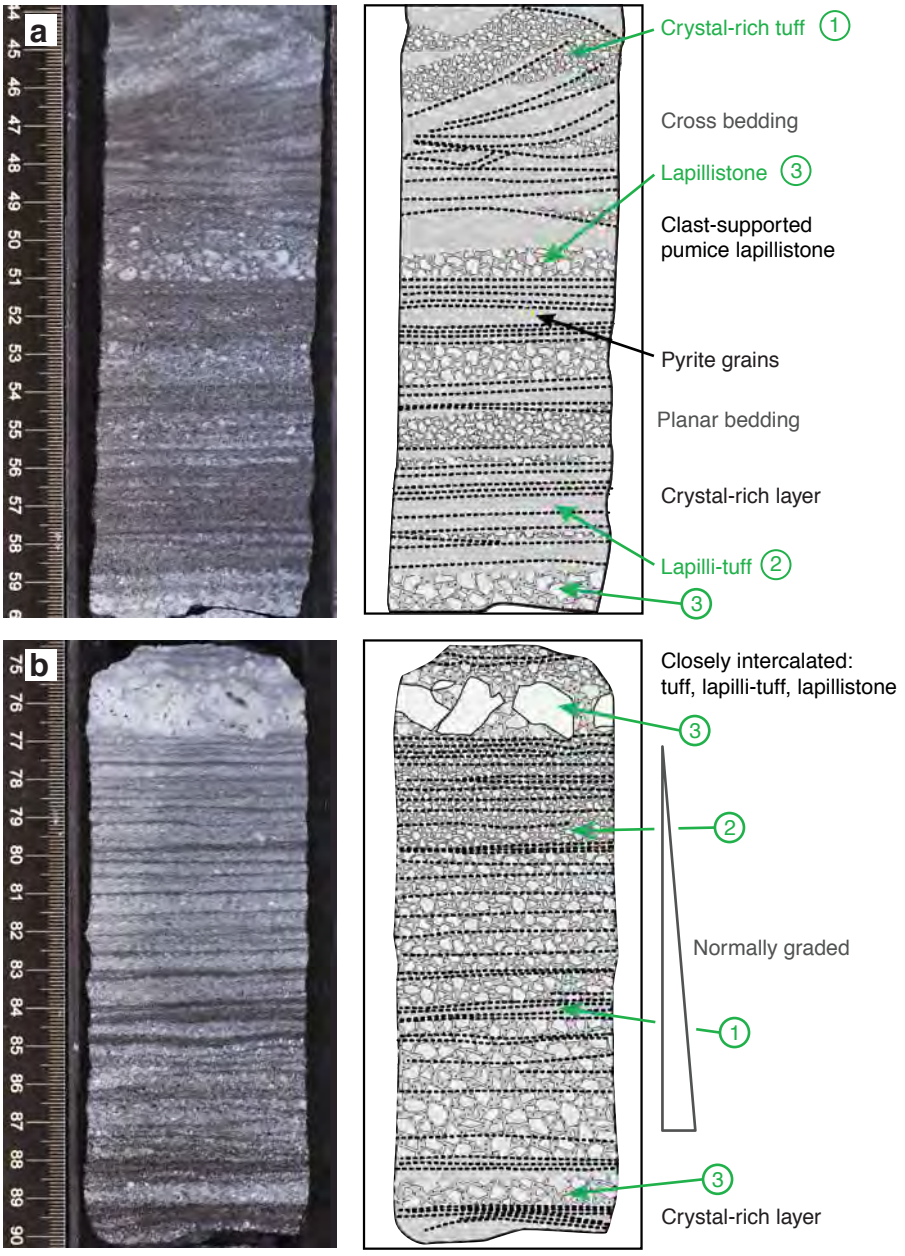
a
b
Crystal-rich tuff 1
Cross bedding
Lapillistone 3
Clast-supported
pumice lapillistone
Pyrite grains
Planar bedding
Crystal-rich layer
Lapilli-tuff 2
3
Closely intercalated:
tuff, lapilli-tuff, lapillistone
3
2
Normally graded
1
3
Crystal-rich layer

Figure 12

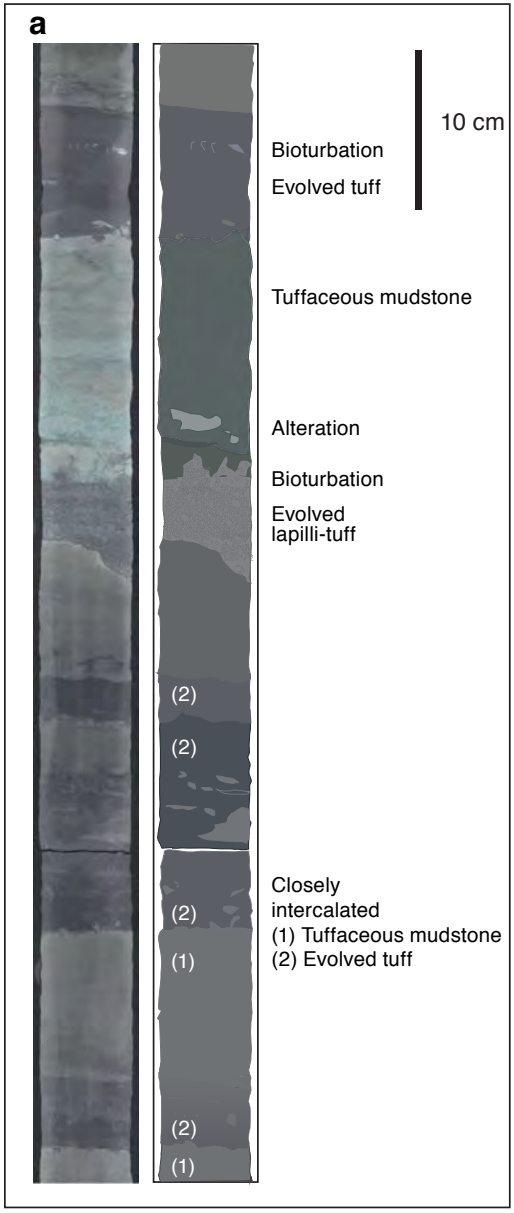
a
10 cm
Bioturbation
Evolved tuff
Tuffaceous mudstone
Alteration
Bioturbation
Evolved
lapilli-tuff
(2)
(2)
(2)
(1)
Closely
intercalated
(1) Tuffaceous mudstone
(2) Evolved tuff
(2)
(1)


b
Intercalated white
to gray/green
evolved tuff
Soft-sediment
deformation

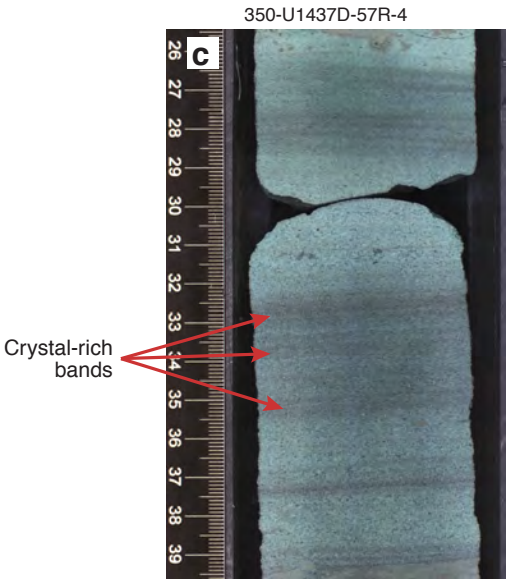
350-U1437D-57R-4
c
Crystal-rich
bands

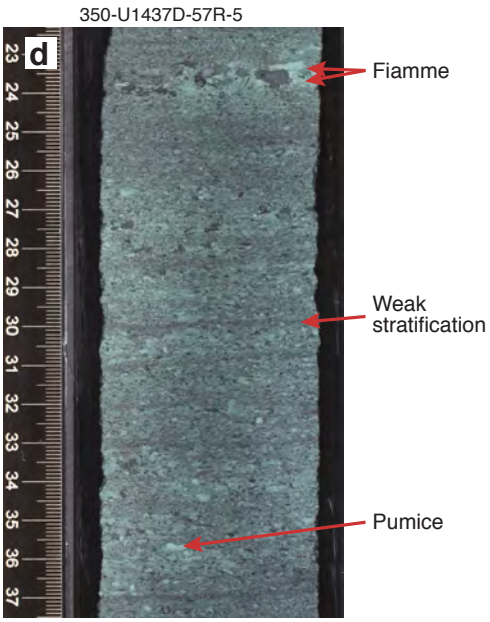
350-U1437D-57R-5
d
Fiamme
Weak
stratification
Pumice

Figure 13

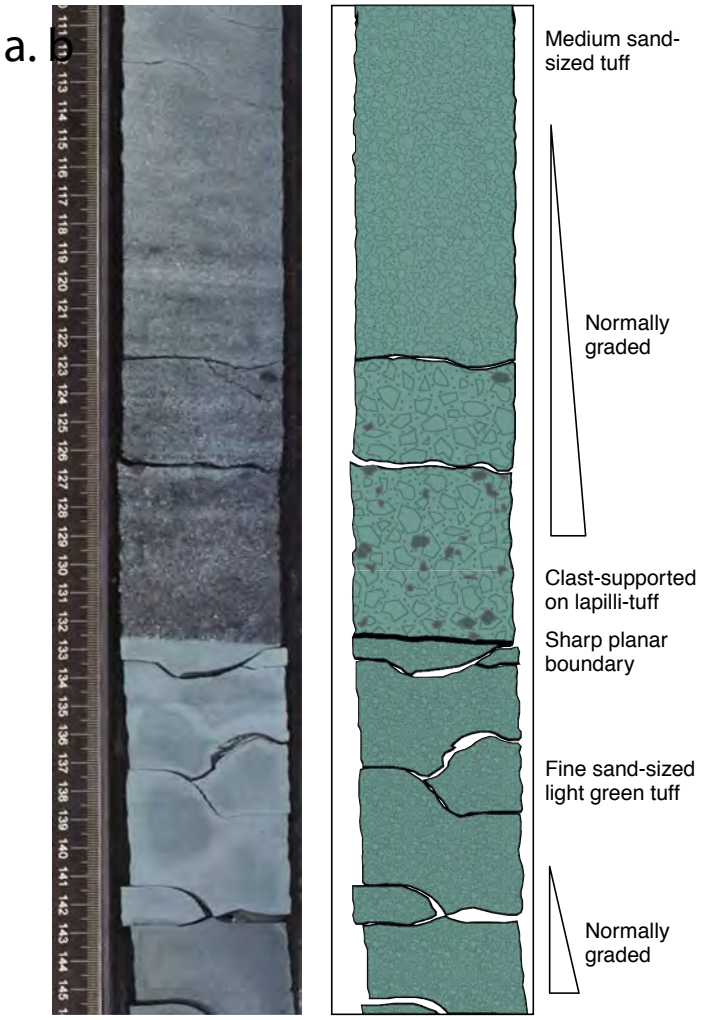
a.
Medium sand-sized tuff
Normally graded
Clast-supported on lapilli-tuff
Sharp planar boundary
Fine sand-sized light green tuff
Normally graded

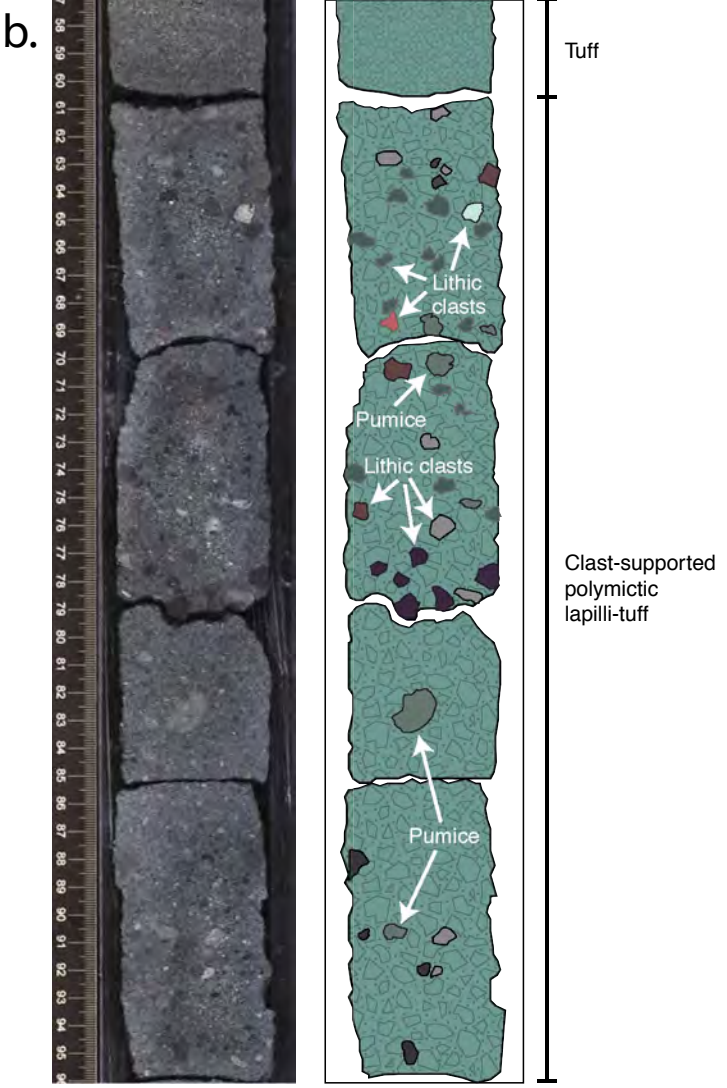
b.
Tuff
Lithic clasts
Pumice
Lithic clasts
Pumice
Clast-supported polymictic lapilli-tuff


c.
350-U1437E-67R-1
350-U1437E-67R-3
1
2

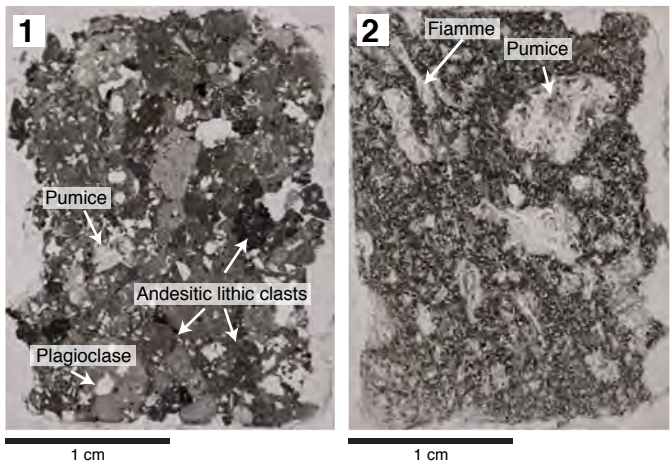
d.
1
Pumice
Andesitic lithic clasts
Plagioclase
1 cm
2
Fiamme
Pumice
1 cm

Figure 14

Figure 15

a.

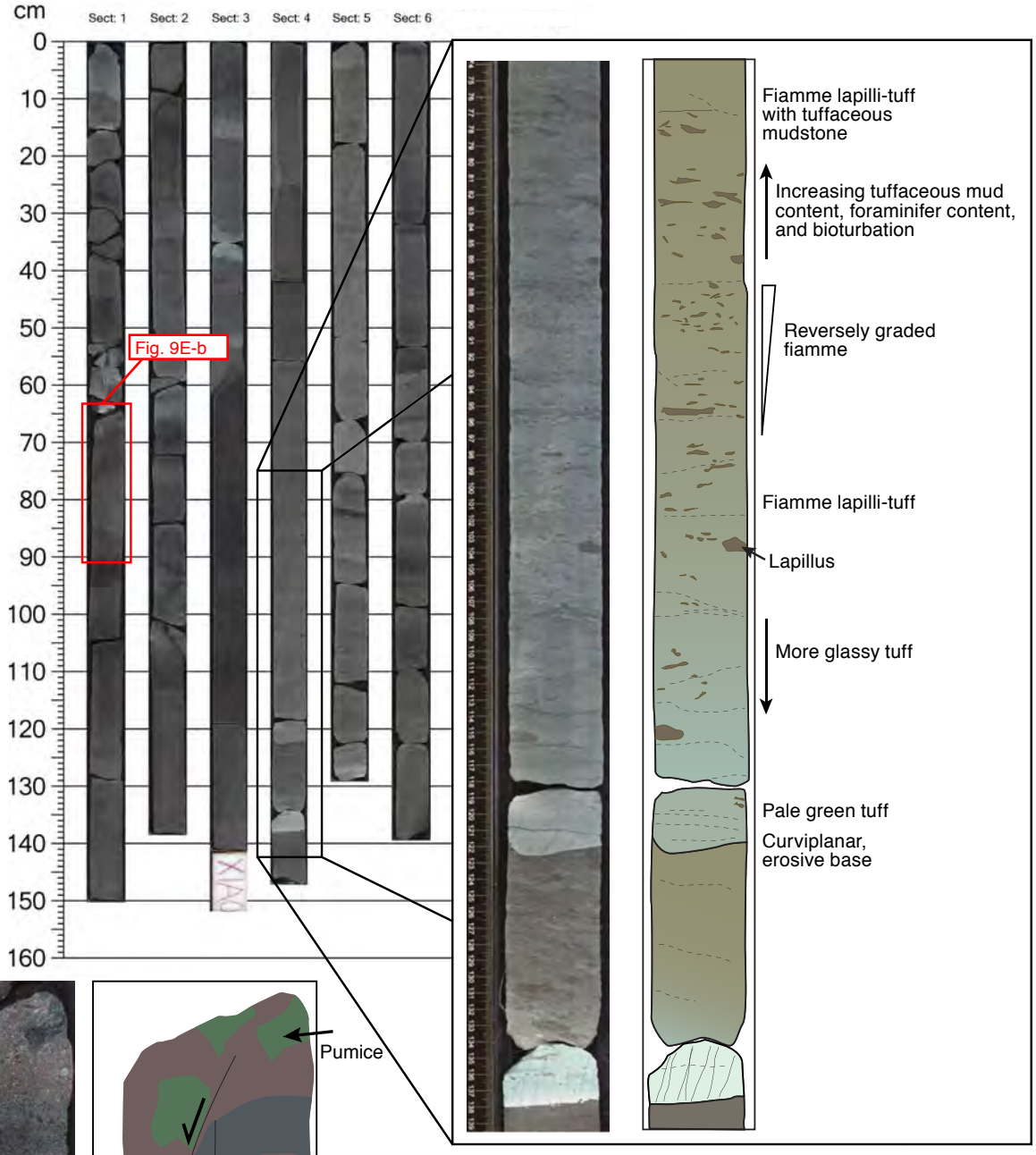

b.

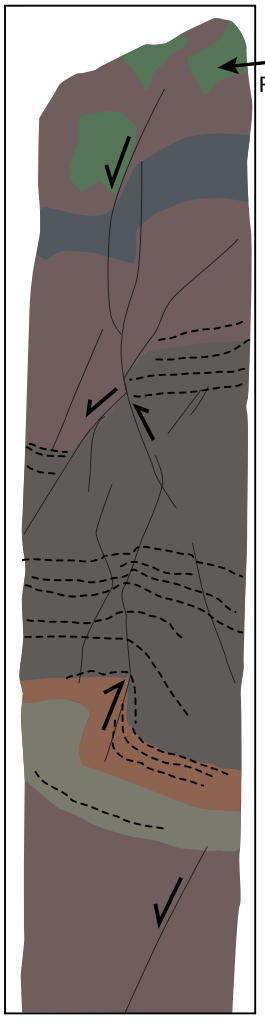

C.

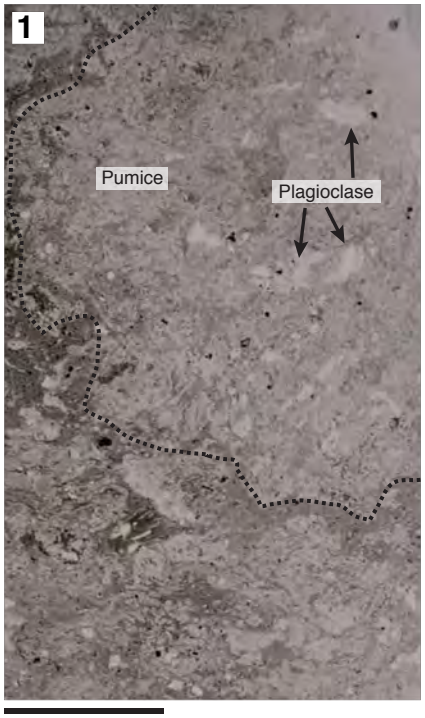

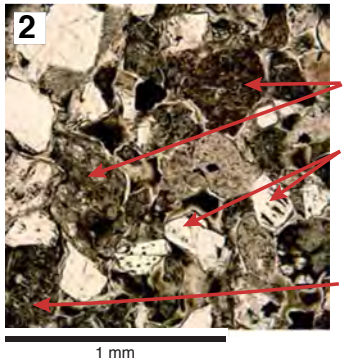

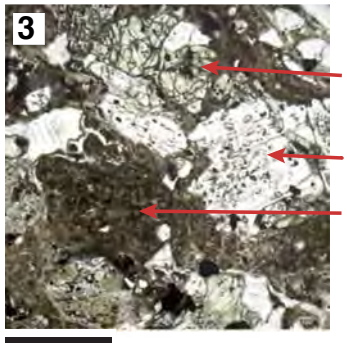

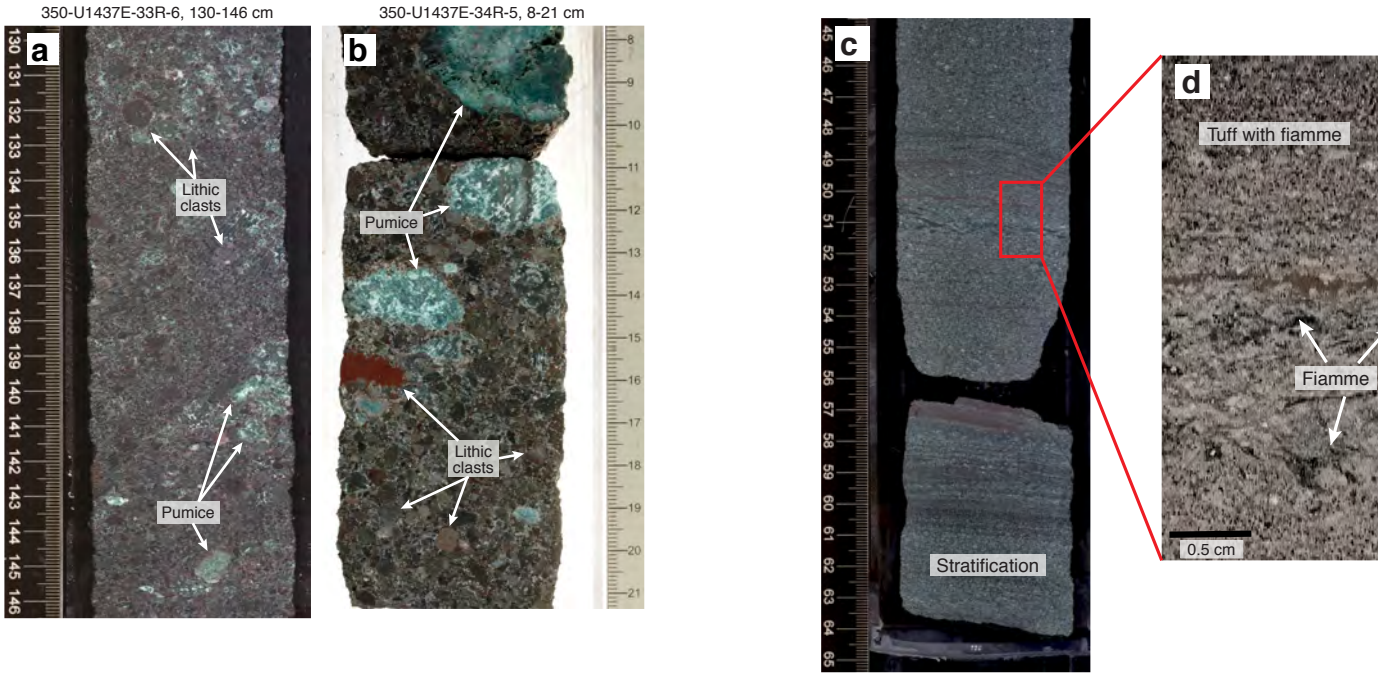
350-U1437E-33R-6, 130-146 cm
350-U1437E-34R-5, 8-21 cm
a
Lithic clasts
Pumice
b
Pumice
Lithic clasts
c
Stratification
d
TS130
Tuff with fiamme
Fiamme
0.5 cm
e
Clast-supported polymictic lapilli-tuff
Lithic clasts
Up
1 cm
f
Matrix-supported polymictic lapilli-tuff
Pumice
Lithic clasts
Up
1 cm
g
h, i
Up
1 cm
h
Clinopyroxene
Plagioclase
Opaque minerals
1 mm
i
1 mm

Figure 16

a.

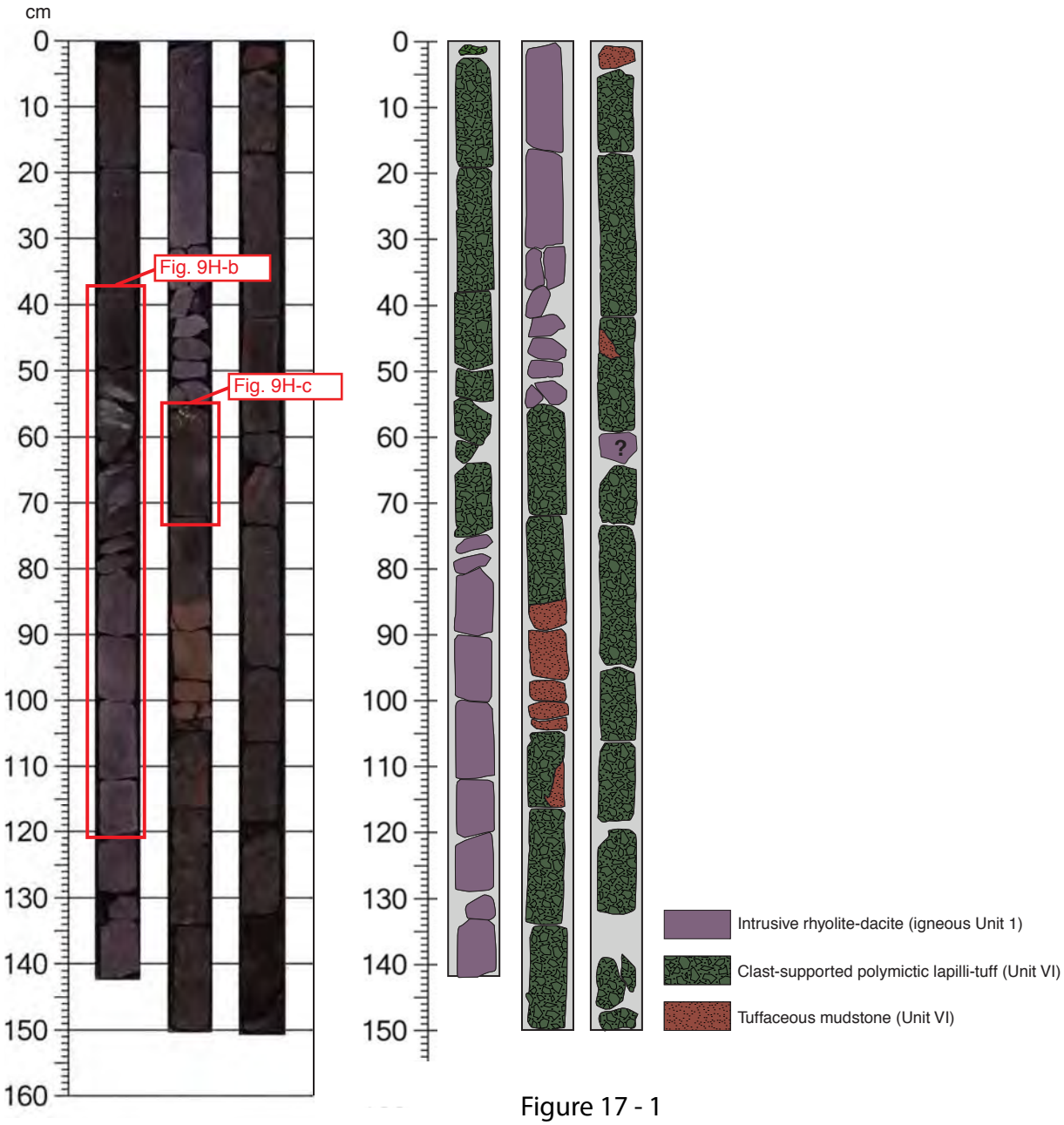
cm
0
10
20
30
40
50
60
70
80
90
100
110
120
130
140
150
160
Fig. 9H-b
Fig. 9H-c
?
Intrusive rhyolite-dacite (igneous Unit 1)
Clast-supported polymictic lapilli-tuff (Unit VI)
Tuffaceous mudstone (Unit VI)

Figure 17 - 1

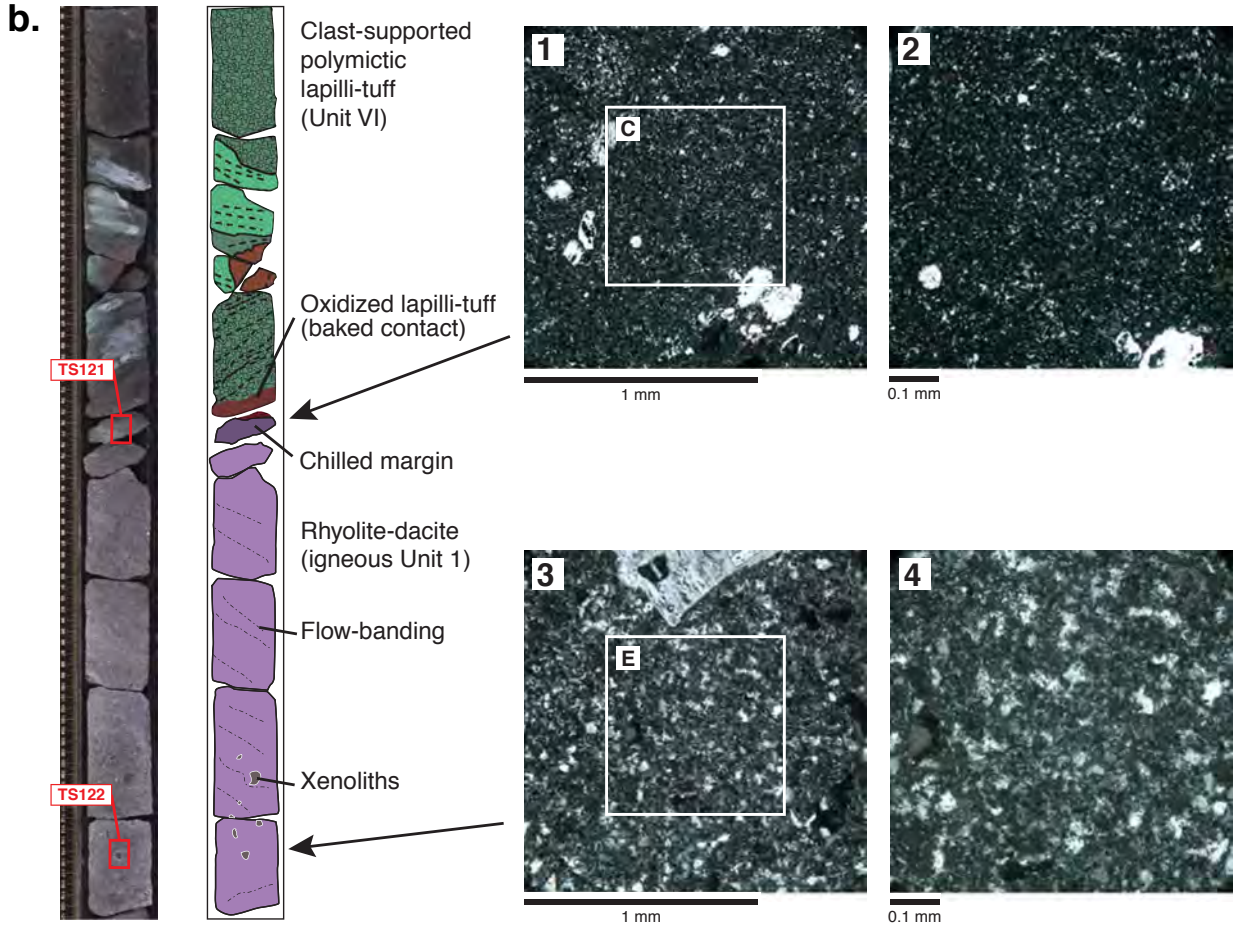
b.
Clast-supported polymictic lapilli-tuff (Unit VI)
Oxidized lapilli-tuff (baked contact)
Chilled margin
Rhyolite-dacite (igneous Unit 1)
Flow-banding
Xenoliths
TS121
TS122
1
C
1 mm
2
0.1 mm
3
E
1 mm
4
0.1 mm

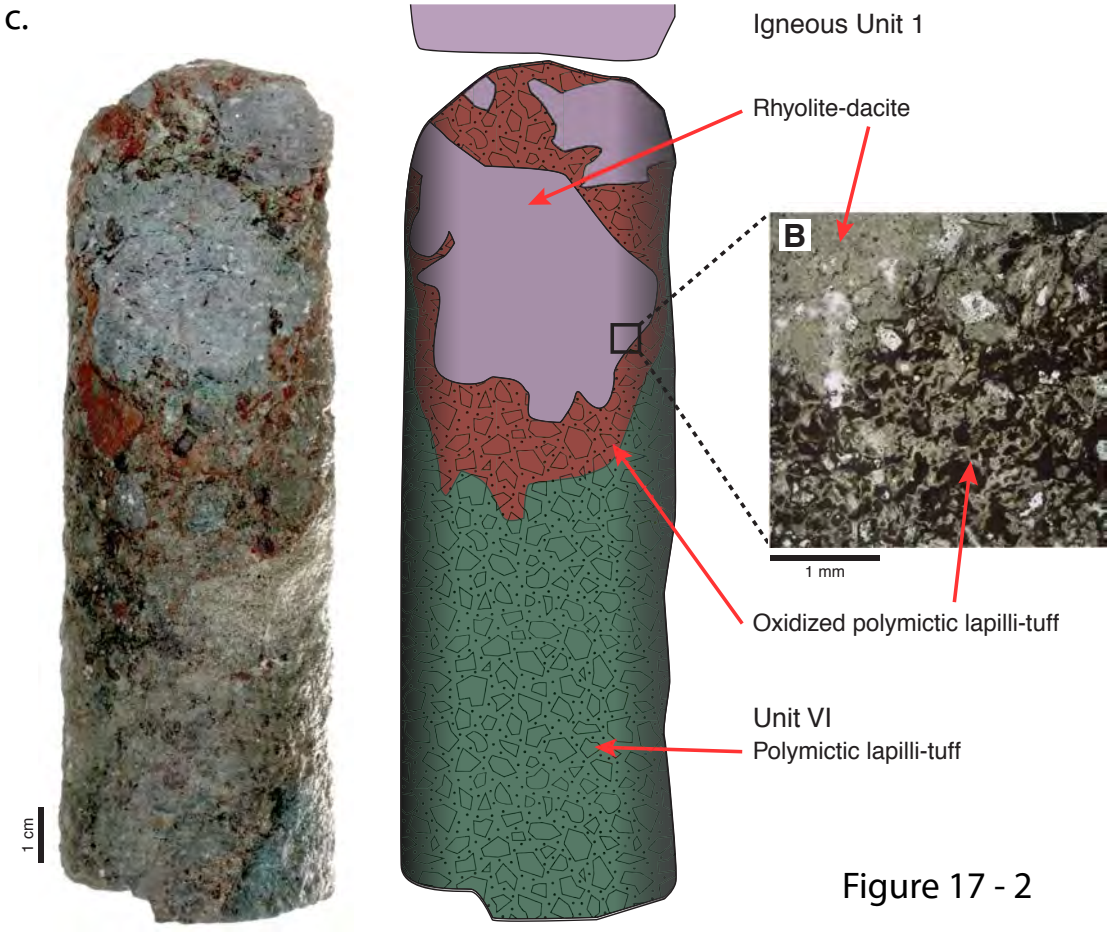
c.
Igneous Unit 1
Rhyolite-dacite
B
1 mm
Oxidized polymictic lapilli-tuff
Unit VI
Polymictic lapilli-tuff
1 cm

Figure 17 - 2

a.

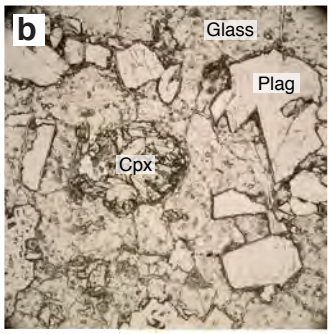

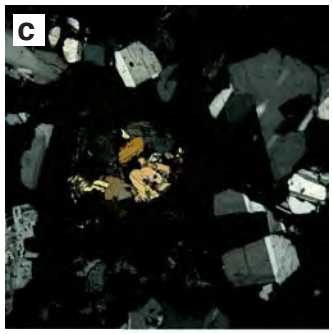

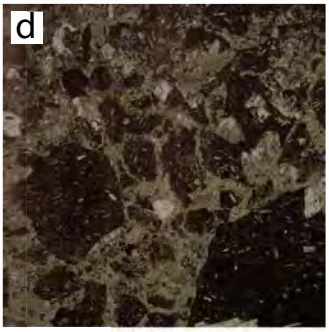

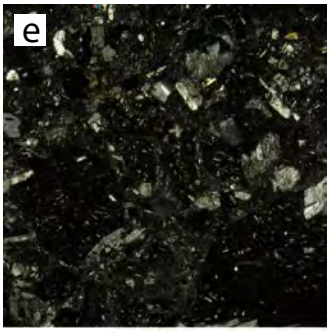

f.

Matrix-supported lapilli-tuff and lapillistone

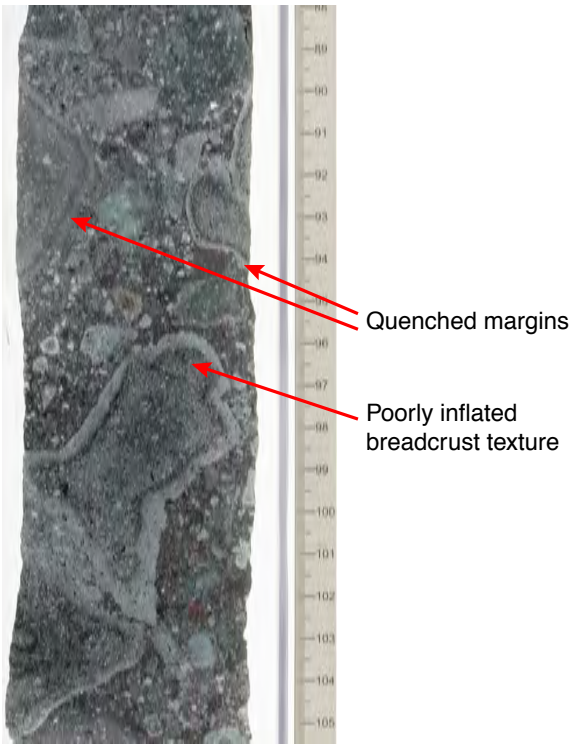

g.

Figure 18

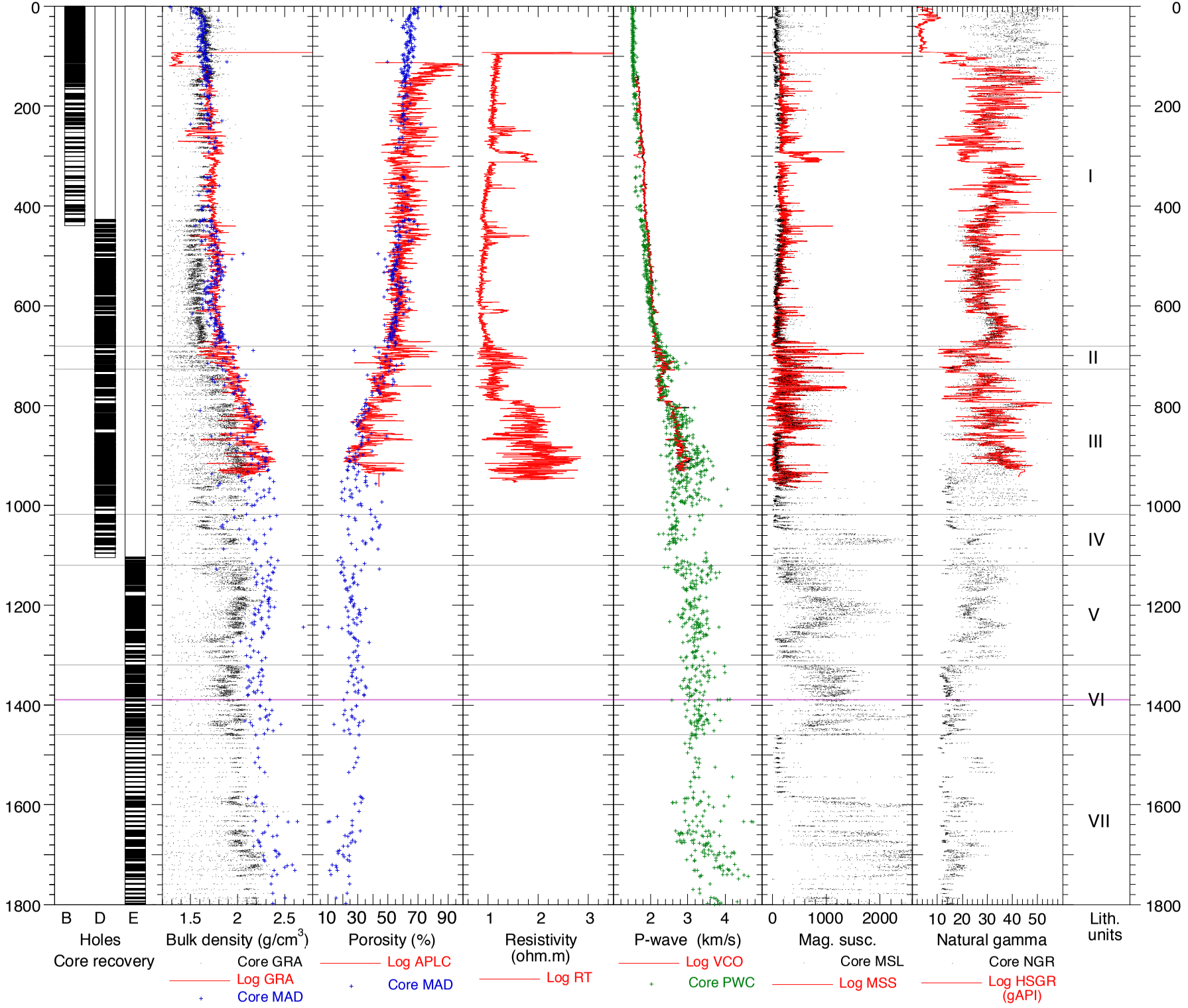
0
200
400
600
800
1000
1200
1400
1600
1800
B
D
E
Holes
Core recovery
1.5
2
2.5
Bulk density (g/cm3)
Core GRA
Log GRA
Core MAD
10
30
50
70
90
Porosity (%)
Log APLC
Core MAD
1
2
3
Resistivity (ohm.m)
Log RT
2
3
4
P-wave (km/s)
Log VCO
Core PWC
0
1000
2000
Mag. susc.
Core MSL
Log MSS
10
20
30
40
50
Natural gamma
Core NGR
Log HSGR (gAPI)
I
II
III
IV
V
VI
VII
Lith. units

Figure 19

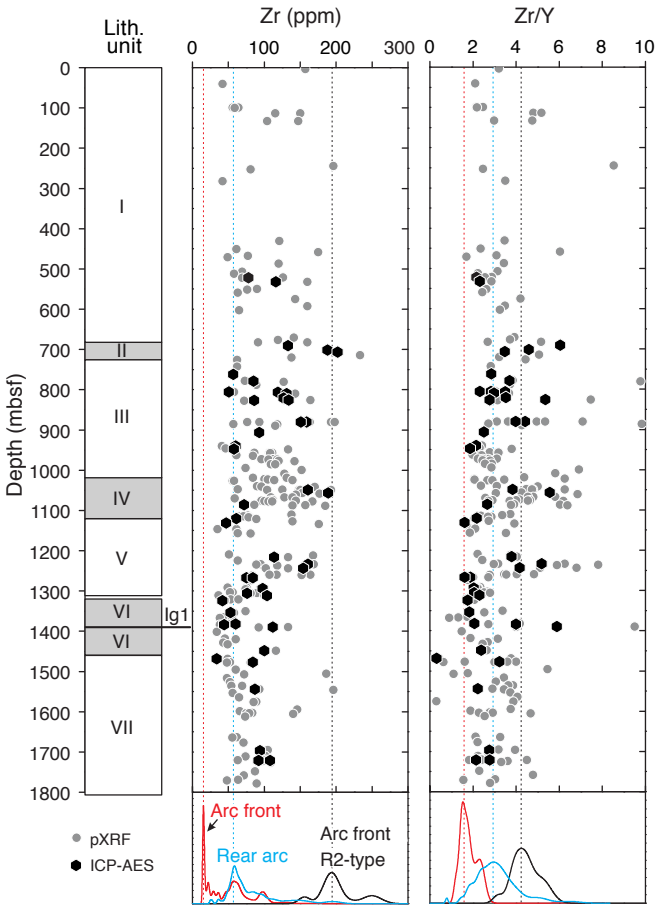
Lith. unit
Zr (ppm)
Zr/Y
Depth (mbsf)
I
II
III
IV
V
VI
VI
VII
lg1
pXRF
ICP-AES
Arc front
Rear arc
Arc front
R2-type

Figure 20

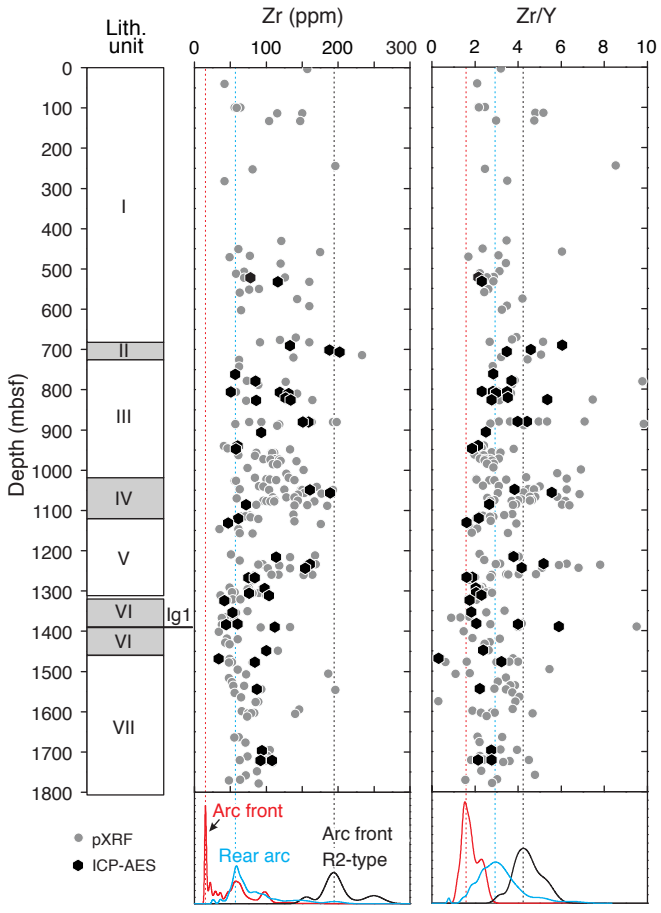
Lith. unit
Zr (ppm)
Zr/Y
Depth (mbsf)
I
II
III
IV
V
VI
VI
VII
lg1
pXRF
ICP-AES
Arc front
Rear arc
Arc front
R2-type

Figure 21